Thesis for the degree of Licentiate of Engineering

Observations with *Herschel*: High-mass star formation and the search for NH^+

MITRA HAJIGHOLI

Department of Earth and Space Sciences
CHALMERS UNIVERSITY OF TECHNOLOGY
Gothenburg, Sweden 2014

Observations with *Herschel*: High-mass star formation and the search for NH^+

MITRA HAJIGHOLI

Radio Astronomy & Astrophysics Group
Department of Earth and Space Sciences
Chalmers University of Technology
SE–412 96 Gothenburg, Sweden
Phone: +46 (0)31–772 1000

Contact information:
Mitra Hajigholi
Onsala Space Observatory
Chalmers University of Technology
SE–439 92 Onsala, Sweden

Phone: +46 (0)31–772 5542
Fax: +46 (0)31–772 5590
Email: mitra.hajigholi@chalmers.se

Front cover: An illustration of the *Herschel* Space Telescope in the upper left corner. In the right upper corner is the massive star forming region G34.26+0.15 localized in the Milky Way (credit:NASA/JPL-Caltech/R). The first zoom in is the Spitzer-GLIMPSE image of the nebulae, it is located in. The second is the continuum map at 24 GHz, superimposed on the PAH emission map (at 8 μm). The spectra is observed towards G34.26+0.15 and is further described in Paper II, appended in this thesis.

Printed by Chalmers Reproservice
Chalmers University of Technology
Gothenburg, Sweden 2014

Observations with *Herschel*: High-mass star formation and the search for NH^+

MITRA HAJIGHOLI
Department of Earth and Space Sciences
Chalmers University of Technology

Abstract

The capture and interpretation of the electromagnetic radiation we receive from space is essential to our understanding of the cosmos. When the Earth's opaque atmosphere prevents the far-infrared radiation to reach ground based antennas, space observatories become crucial to collect that important piece of the large puzzle that otherwise would have been lost. In this thesis, we use observations of light hydrides in the far-infrared performed with the *Herschel* Space Observatory and its sensitive instrument the Heterodyne Instrument for the Far-Intrared (HIFI). The goal is to increase our understanding of the physical and chemical conditions present in the interstellar medium (ISM) – the gas and dust between stars in galaxies – and how massive stars are able to form deep within the extremely large and ice cold gas clouds in the ISM.

In Paper I, we present searches for a so far undetected key molecule in the interstellar nitrogen chemistry, NH^+, along with the anion NH_2^-. Despite the most sensitive searches up to date, no detections were made. The upper limits are, however, used to constrain chemical models of different cloud types in the ISM.

High spectral resolution observations of the ammonia molecule in the far-infrared are used in Paper II to analyze the early phases of massive star formation. Due to the scarce number of massive stars forming in the Galaxy, typically at vast distances, several competing theories exist in massive star formation theory. Our multi-transitional observations of ammonia spectral lines allowed a detailed modeling of the accretion process in the massive star forming region G34.26+0.15 at a distance of 3.3 kpc. With the use of an accelerated lambda iteration code to model the observed line profiles, the radial distribution of the density, temperature and velocity field, as well as the ammonia abundance and ratio of its ortho and para symmetry forms, were deduced. The usage of seven rotational ammonia transitions probing different layers of the collapsing cloud allowed a detection of two cloud components moving inwards toward the central region of the massive star forming cloud. Our results do not agree with previous published results suggesting a free-fall collapse of a single cloud, based on only a few observed transitions. The mass accretion rates are found to be high enough to overcome the expected radiation pressure from G34.26+0.15 and support the competitive accretion process in high-mass star formation theory.

Keywords: High-mass star: formation – ISM: abundances – ISM: molecules – ISM: individual objects: G10.6-0.4, Sgr B2(M) and G34.26+0.15 – Radio lines: ISM – Submillimeter – Line: profiles – Line: formation

List of Appended Papers

This thesis is based on the work contained in **Papers I** & **II**:

I Carina M. Persson, M. Hajigholi, G.E. Hassel, A.O.H. Olofsson, J.H. Black, E. Herbst, H.S.P. Müller, J. Cernicharo, E.S. Wirström, M. Olberg, Å. Hjalmarson, D.C. Lis, H.M. Cuppen, M. Gerin, K.M. Menten
Upper limits to interstellar NH^+ and para-NH_2^- abundances
Herschel-HIFI observations towards Sgr B2 (M) and G10.6−0.4 (W31C)
Astronomy & Astrophysics, submitted 4 March (2014)

II Mitra Hajigholi, C.M. Persson, E.S. Wirström, J.H. Black, P. Bergman, A.O.H. Olofsson, M. Olberg, F. Wyrowski, V. Taquet, A. Coutens, Å. Hjalmarson and K.M. Menten
Observational support of competitive accretion model for high-mass star formation
A multi-transitional THz Herschel-*HIFI study of ammonia toward G34.26+0.15*
Astronomy & Astrophysics, to be submitted (2014)

Other Publications

I have also participated in the following paper not included in the thesis:

Joachim Wiegert, R. Liseau, P. Thébault, G. Olofsson, A. Mora, G. Bryden, J. P. Marshall, C. Eiroa, B. Montesinos, D. Ardila, J. C. Augereau, A. Bayo Aran, W. C. Danchi, C. del Burgo, S. Ertel, M. C. W. Fridlund, M. Hajigholi, A. V. Krivov, G. L. Pilbratt, A. Roberge, G. J. White, and S. Wolf
How dusty is α Centauri? Excess or non-excess over the infrared photospheres of main-sequence stars
Astronomy & Astrophysics, 563, A102 (2014)

Acknowledgements

I would like to thank everyone who believed in me, including my self, and helped me get to this stage in my career. This thesis would not have been possible without the kind support of many people, especially my three supervisors. First of all I would like to thank my inspiring supervisor Carina Persson, who I certainly would not have managed without. I have learned so much from you. Thank you my second supervisor John Black for his infinite wisdom and always being helpful and friendly to me. Thank you also my third supervisor Eva Wirström who always been a great support through my work and who I had many laughters with. Thank you all for your patient, help and encouragement. I have really enjoyed our discussions and work. Thank you Per Bergman, your support has improved the quality of this thesis significantly. Thank you Åke Hjalmarsson and Henrik Olofsson for your comments on this thesis.

I also would like to thank everybody at the department giving me that extra energy and great support, especially my fellow past and present PhD students with who I had unforgettable memories. Thank you Roger, Michael and Glenn for always being awesomely helpful. I also would like to take the opportunity to thank the beautiful and peaceful geological position chosen for Onsala Space Observatory, offering us unbeatable scenery every day at work.

Thank you to all my collaborators, for sharing their knowledge and broadening mine. I really feel lucky to work in such a great team of scientist, both at Onsala but also with people all around the world. I am grateful for the generous support from the Swedish Research Council (SRC) and the Swedish National Space Board (SNSB).

Last but not least, thank you my lovely family, and Johan, for their endless support and love.

Mitra

Onsala, May 2014

Contents

Chapter 1

Introduction

The introduction to this thesis begins with the most essential component of galaxies – the gas and dust between stars referred to as the interstellar medium (ISM). The ISM is a very important component of galaxies since it is here that the dominant sources of energy - stars - are forming. Our knowledge about the ISM is mainly based on the interpretation of the electromagnetic radiation which is radiated by atoms, molecules, ions and dust grains and captured by large radio antennas. The thesis therefore continues with an overview of the general principles governing the energy-level structure of molecules, absorption and emission of radiation by molecules, and how this radiation can be detected. The main focus of this thesis - star formation - is then presented in chapter two, including theories explaining how the extremely thin and cold gas can turn into extremely dense and hot stars. In contrast to low-mass star formation, the understanding of massive star formation is still far from complete. Several competing theories exist while few observations have been performed to test the formation theories. An overview of radiative transport is then outlined, in addition to different ways to model the propagated radiation along the line of sight. Finally, the thesis ends with an introduction to each appended paper.

1.1 Interstellar medium

General references: Tielens (2010); Hartquist & Williams (1995); Snow & McCall (2006)

Along the Milky-Way's spiral arms, the dynamic interstellar medium is stretched out and sprinkled with new born stars. In this ever changing environment, galactic evolution takes place. It is an unusual chemical and physical laboratory, characterized by very low densities and temperatures not available on Earth[1]. Therefore,

[1]The density of the air we breathe is approximately 3×10^{19} molecules per cm^{-3} and that of the best man-made vacuum on the Earth surface is reported to be, to date, about $10^3\,\mathrm{cm}^{-3}$.

species which are highly reactive and chemically unstable on Earth can be quite abundant in the ISM. For instance, the spectral line radiation from the molecular ion HCO^+ (Klemperer, 1970) was observed (Buhl & Snyder, 1970) in the ISM before it could be synthesized in detectable quantities in laboratories (Woods et al., 1975) on Earth.

At the same time as the ISM is the birthplace of stars and planets, the bright stars regulate the structure, composition and chemical evolution of the ISM, thus influencing the star formation rate and galactic evolution. In a cyclic process, gas and dust clouds collapse gravitationally to form stars which in the end of their lives eject gas and dust back to the ISM. The gas is, however, at this point enriched with small amounts of elements heavier than helium, produced by the stars.

The ISM is observable by means of its emission lines and absorption of radiation that travels though it. However, the analysis of the lines becomes complicated since the signals often are very weak and difficult to detect, and the ISM is also far from equilibrium.

The ISM we observe at the present epoch is a mixture of 99 % gas and 1 % dust, by mass. Approximately three quarters of the gas mass is in the form of atomic or molecular hydrogen and one quarter of helium. In addition, $1 - 2$ % of the gas mass consists of species heavier than helium, for instance carbon, nitrogen and oxygen. These elements are produced by thermonuclear processes in the hot cores of stars, and by neutron capture processes in old and dying stars. One of the most important processes is the proton-proton chain in which four protons are combined into one helium nucleus through a series of reactions. This process is efficient at temperatures above 10 million K and is presently producing the energy of our sun. Synthesis of even heavier elements (up to iron) takes place at much higher temperatures. For instance the triple-alpha process, in which carbon is produced, requires temperatures above 100 million degrees Kelvin (K). In both these processes heavy elements - and energy - are produced from light elements. Elements heavier than iron cannot, however, be synthesized similarly since these elements demand energy for their production. They are instead synthesized by neutron capture in which heavier elements are produced when an atomic nucleus and one or more neutrons collide and merge. The process can proceed in two ways: rapid neutron capture (r-process) which takes place in the moments when a massive star explodes as a supernova, or slow neutron capture (s-process) primarily occurring in the envelopes of old stars, the "Asymptotic Giant Branch" (AGB) stars, where the neutron density and temperature are relatively low. The s-process is responsible for the production of approximately half the abundances of elements heavier than iron in the Galaxy. The dispersed elements, by e.g. stellar mass loss or winds, planetary nebulae or supernova explosions, are later incorporated into stars and planetary systems.

The ISM is highly non-homogeneous and shows structure on all scales. Depending on the environment the gas may be ionized, atomic or molecular. Different

types of clouds cover a wide range of temperatures, densities and sizes. Several classifications of cloud types exist and one classification (related to the visual extinction A_V) of the cold gas in the ISM is diffuse atomic, diffuse molecular, translucent and dense molecular clouds (summarized in Table 1.1). In addition, there also exist warm, neutral or ionized gas ($T \approx 6000 - 10\,000$ K) and hot, ionized gas ($T \sim 10^6$ K) where the different cloud types are in rough pressure equilibrium with each-other. The hottest gas has extremely low densities ($n_H \lesssim 1$ cm^{-3}) but occupies most of the volume of the Galaxy. This cloud type will, however, not be further discussed in this thesis. In the classification of the cold gas, which contains most of the ISM mass, *the diffuse atomic clouds* represent the lowest density regime in the cold ISM where nearly all molecules are photo-dissociated into atoms or ions. Photo-dissociation occurs when the molecular fraction is too low to prevent the penetration of ultraviolet (UV) photons from massive stars. *The diffuse molecular clouds* represent a slightly denser regime where the interstellar radiation field is attenuated, but still strong enough to photo-dissociate carbon monoxide (CO), keeping most of the carbon in the form of C^+. In steady state, the diffuse atomic gas surrounds the diffuse molecular gas and serves as a shield from external radiation. *Translucent clouds* represent an even denser gas, being sufficiently protected from interstellar radiation by both the embracing diffuse atomic and diffuse molecular clouds. As a result, more complex molecules can form and the dominant forms of carbon is here in C and CO. *Dense molecular clouds* are typically self-gravitating and represent a regime were the density and extinction is high enough to completely make carbon molecular. Here the electron abundance is very low and cosmic rays are the dominant ionizing source. Note that despite the convenient classifications, most sight-lines likely consist of a mixture of different types of clouds. The above cloud types can therefore be regarded to reflect *local* conditions of the gas.

Table 1.1: Classification of interstellar cloud types and their corresponding typical values of minimum extinction, $A_{V,min}$(mag); density, n_H(cm^{-3}); and temperature, T(K). The techniques used to observe these regions are presented, such as emission (em), absorption (abs) lines in the ultra violet (UV), visual (Vis), infrared (IR) or millimeter (mm) regime. Table adapted from Snow & McCall (2006).

	Diffuse Atomic	Diffuse Molecular	Translucent	Dense Molecular
$A_{V,min}$	0	~ 0.2	$\sim 1-2$	$\sim 5-10$
n_H	$10-100$	$100-500$	$500-5000$	$>10^4$
T	$30-100$	$30-100$	$15-50$	$10-50$
Observ.	UV/Vis	UV/Vis IR abs	Vis (UV) IR abs	IR abs
Techniq.	H I 21-cm	mm abs	mm abs/em	mm em

Molecules can be produced in several ways, but their formation processes can be separated into two broad classes: reactions that occur in the gas phase and reactions that occur on the surfaces of small grains. Gas phase reactions (listed in Table 1.2) can be divided into three different categories reflecting their reaction effects. The first process bonding atoms into simple or more complex species with radiative association or associative detachment. The second represents reactions that fragment species into smaller species, such as photodissociation, dissociative recombination, and collisional dissociation. Finally, there are the bond-rearrangement reactions such as the charge-transfer reactions and neutral-neutral reactions, which transfer parts of one coreactant to another one.

Table 1.2: Gas phase reactions types (Tielens, 2010).

	reaction
Photodissociation	$AB + h\nu \rightarrow A + B$
Neutral-neutral	$A + B \rightarrow C + D$
Ion-molecule	$A^+ + B \rightarrow C^+ + D$
Charge-transfer	$A^+ + B \rightarrow A + B^+$
Radiative association	$A + B \rightarrow AB + h\nu$
Dissociative recombination	$A^+ + e \rightarrow C + D$
Collisional association	$A + B + M \rightarrow AB + M$
Associative detachment	$A^- + B \rightarrow AB + e$

Silicates, graphite, and carbides, the most important building blocks of dust particles with a size of $0.01\,\mu\text{m} - 1\,\mu\text{m}$, condense in the dense and warm envelopes of old (AGB) stars, or in similar environments created by e.g. a supernova. Dust grains play a very important role in interstellar chemistry for many reasons. One is by acting as a catalyst for molecule formation. Once an atom or molecule is attached to a grain the probability to find another atom or molecule to react with increases dramatically compared to the gas phase. In cold and dense clouds, the gas-phase species can accrete onto the dust grains to form an icy mantle consisting of simple molecules such as water (H_2O), CO, carbon dioxide (CO_2), and methanol (CH_3OH) thereby increasing the grain size. Ultraviolet radiation and high-energy cosmic rays can also reprocess the ices producing even larger and more complex molecules. When heated, the dust particles may lose their mantles and the molecules return to the gas phase. This process is often referred to as thermal desorption. More energetic events, such as shocks driven by e.g. powerful stellar winds or supernova explosions can cause sputtering of molecules off the dust grains or completely shatter the grains into smaller pieces. Another important grain property of the dust particles is the shielding of the interior parts of a cloud which enables molecules to survive in the deep interior. The dust shielding controls

the extinction ($A_{\rm V}$) of starlight passing though the interstellar clouds by absorbing and scattering energetic photons having λ shorter than the size of the grain. When absorbing stellar UV and visible radiation the dust grains are heated and radiate at infrared wavelengths which in turn is heats the molecules. Regions where the dust efficiently blocks the light from background stars are traditionally known as dark clouds (more in Chapter 2). The relation between the total extinction measured at wavelengths in the V-band[2], $A_{\rm V}$ (measured in magnitudes), and the column density of neutral hydrogen atoms, $N_{\rm H}$ (measured in cm^{-2}), measured in the Milky Way (Stahler & Palla, 2005), shows how the gas and dust in the ISM are related:

$$\frac{N_{\rm H}}{A_{\rm V}} \approx 5.3 \times 10^{22} \text{ atoms cm}^{-2} \text{ mag}^{-1}. \tag{1.1}$$

A high extinction thus implies that a large amount of radiation has been blocked by gas and dust in the line of sight. The column density is defined as (more in Sect. 3)

$$N = \int n \, ds \ , \tag{1.2}$$

where n is the volume number density and s is the path-length.

1.2 Molecular emission and absorption

General references: Tielens (2010); Rohlfs & Wilson (1996)

Our understanding of the ISM is built upon observations of interstellar ions, atoms and molecules, and the study of their formation routes (astrochemistry). Even though the interstellar clouds are located at extreme distances – one of the closest massive star forming regions (the Orion Nebula) is located at a distance of 100 million AU[3] – more than 175 interstellar molecules have been identified so far[4]. This number is steadily increasing thanks to the development of much improved antennas (both at ground and in space), receivers and laboratory spectroscopy. The weak electromagnetic radiation produced by the observed species travels all the way through the ISM towards Earth. Along the way the radiation can be absorbed or deflected through various interactions, or more emission may be added to the beam before finally reaching our detectors. (More on radiative transfer in Chapter 3.)

[2]V-band stands for the visual photometric band which corresponds to a relatively broad wavelength interval with effective width 890 Å; centred on 5500 Å, where Å(Ångströms) is a unit for length equal to 10^{10} m

[3]One AU is the average distance between the Earth and the Sun, equal to about 1.5×10^{11} m.

[4]see e.g. cdms: `http://www.astro.uni-koeln.de/cdms/molecules` or the website at Astrochymst: `http://www.astrochymist.org/astrochymist_mole.html` having a regularly updated list that has links to discovery papers.

Molecules are excellent probes of the chemistry and physical conditions in interstellar clouds. The total internal energy of a molecule is the sum of the electronic, vibrational, and rotational energies. An electronic transition occurs when a valence electron jumps between electronic energy states, emitting at energy levels of a few eV corresponding to the UV or visual regions of the electromagnetic (EM) spectrum. Vibrational transitions are caused by oscillations of the relative positions of the nucleus with respect to their equilibrium positions, emitting at energy levels of $0.1 - 0.01$ eV[5] with typical wavelength of a few μm (infrared EM radiation). Rotational transitions are caused by changes of the rotation around the molecular rotation axes, with typical energies of $\sim 10^{-3}$ eV corresponding to lines in the sub-millimeter to cm wavelength range. In this thesis, only rotational transitions of linear and symmetric-top molecules are considered with a special focus on ammonia rotational transitions at THz frequencies.

The energy separation between each rotational level, denoted by the quantum number of angular momentum J is, well matched to the typical energies available in molecular clouds. The population of the energy levels is determined by competing processes such as collisions with atoms, molecules and ions, absorption and emission of radiation and scattering. Selection rules determine which radiative transitions are allowed. Since the lowest rotational levels of many molecular species have energies of only a few Kelvin above the ground state, transitions between such levels are very suitable to probe the cold molecular gas. Higher rotational states may have energy levels of the order of tens or hundreds of Kelvin above the ground state and are thus suitable to probe warm molecular gas.

1.2.1 Rotational excitation

Linear molecules

For a simple linear molecule, for example CO or HCO^+, there is only one rotational quantum number, J, of the angular momentum perpendicular to the line connecting the two or more nuclei. The energy above ground of a rotational state is quantized for a rigid molecule as

$$E = h\, B_0\, J(J+1), \tag{1.3}$$

where h is the Planck's constant and B_0 is the rotational constant, typically on the order of tens GHz. Allowed radiative transitions have $\Delta J = \pm 1$. From equation (1.3) the frequency of such a transition is $\nu = \Delta E/hc = 2\, B_0\, (J+1)$. In the case of a slightly elastic molecule[6], e.g. from centrifugal distortion, small modifications need to be added.

[5] 1 eV $\approx$ 11600 K

[6] A molecule at a lower energy transition are generally defined to have rigid rotational axes, and when the axes of the molecule gets stretched out due to its high angular momentum (at higher energy transitions) it is defined to be a elastic molecule. The centrifugal distortion is not noticed much for low energy transitions (low J) but the effect becomes more pronounced for high J transitions.

Symmetric top molecules

For an arbitrarily shaped molecule, the rotation can be described as the superposition of three free rotations about three principal rotation axes (x, y and z). Symmetric molecules have mirror symmetry at any angle of rotation around one of its axes. In a symmetric top molecule two of three axes have the same moment of inertia. One example of a symmetric top is the ammonia (NH_3) molecule illustrated in Figure 1.1. The rotational levels are denoted by two quantum numbers, the total angular momentum, J, and its projection K onto the molecular symmetry axis written as J_K. Quantum mechanical tunneling can also cause the atom on the rotational symmetry axis to tunnel through the plane by the two rotational degrees of freedom and thus splits each J_K state into a pair of inversion substates as long as $\Delta K \neq 0$.

An example is the tunneling of the nitrogen atom through the plane defined by the three hydrogen atoms in the ammonia molecule (see Figure 1.1) producing inversion transitions at cm-wavelengths. These spectral lines have proven to be particularly useful to probe the density and temperature of molecular clouds and have also been extensively observed since its discovery already in 1968 by Cheung et al. (1968).

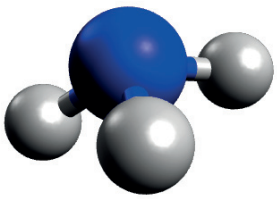

Figure 1.1: The symmetric top ammonia (NH_3)

1.2.2 Interstellar spectra

The frequency pattern is unique for each molecule and reflects the energy separation of a molecule's rotational, vibrational and electronic levels. As a result different molecular species can be identified in the ISM by their spectral line fingerprint. When analyzing astronomical spectra the relative motion between a source and the observer has to be taken into account. If the source is moving at a speed v_s away from an observer at rest the expected emission or absorption of the photons will have their frequency shifted by the Doppler effect to the observed

frequency

$$\nu_{\rm obs} = (1 - \frac{\upsilon_{\rm s}}{c})\,\nu_0, \tag{1.4}$$

where ν_0 is the rest frequency of the emitted (or absorbed) photons. The formula is only valid in the non-relativistic case when $\upsilon_{\rm s} \ll$ c. A negative velocity corresponds to a source moving toward us and a positive velocity a receding source. The frequency scale of molecular lines is often converted to Doppler velocities relative to the local standard of rest ($\upsilon_{\rm LSR}$). An example is shown in Fig. 1 in Paper II, appended in this thesis.

The Doppler effect not only shifts the observed frequency (or $\upsilon_{\rm LSR}$) of a spectral line, it also causes Doppler-broadening of the line profile by e.g. thermal motions and turbulence in the observed region. If the transition is optically thin (see Sect. 3.1) the velocity distribution of the gas will be reflected in the line profile produced, averaged on the telescope's resolution element. If a Gaussian velocity distribution is assumed, of the gas with a dispersion $\sigma_{\rm V}$, the resulting dispersion in frequency will be in the order of $\sigma_\nu = \nu_0\,\sigma_{\rm v}/c$ The typical values of $\sigma_{\rm v}$ due to thermal motion is $\sim$0.5 to a few km s $^{-1}$ and depend on the square root of the kinetic temperature divided by the mass of the molecule. Other even larger broadening effects can be caused by turbulent Doppler broadening (line widths of $\sim$5 to tens of km s $^{-1}$), and by Galactic rotation (line widths of hundreds of km s $^{-1}$).

1.3 Detecting molecular emission and absorption

Emission from molecular rotation occurs in the radio to far-infrared part of the electromagnetic spectrum, corresponding to MHz to THz frequencies. At these frequencies, the Earth's atmosphere is not transparent and absorbs a large part of the radiation, especially at the frequencies corresponding to absorption bands of the most abundant molecules such as H_2O and O_2. However, some spectral windows exist where the atmospheric transmission is sufficiently high to allow mm and sub-millimeter observations from ground. Since the atmospheric transmission strongly depends on the amount of precipitable water vapour (pwv), sub-millimeter-wave observatories need dry sites at high altitudes. A very good example is the Atacama desert at 5000 meters altitude which is the site of the Atacama Large Millimetre Array (ALMA)[7] and APEX (Atacama Pathfinder Experiment)[8] telescopes (Fig. 1.2). Observations at frequencies higher than $\sim$1 THz have to be done above the atmosphere using space observatories. Three examples of successful sub-millimeter space observatories are the Submillimeter Wave Astronomy Satellite (SWAS)[9], the

[7] http://almascience.eso.org/, http://www.nordic-alma.se/
[8] http://www.apex-telescope.org
[9] http://lambda.gsfc.nasa.gov/product/swas/

Swedish Odin[10] satellite and ESA's *Herschel*[11] mission.

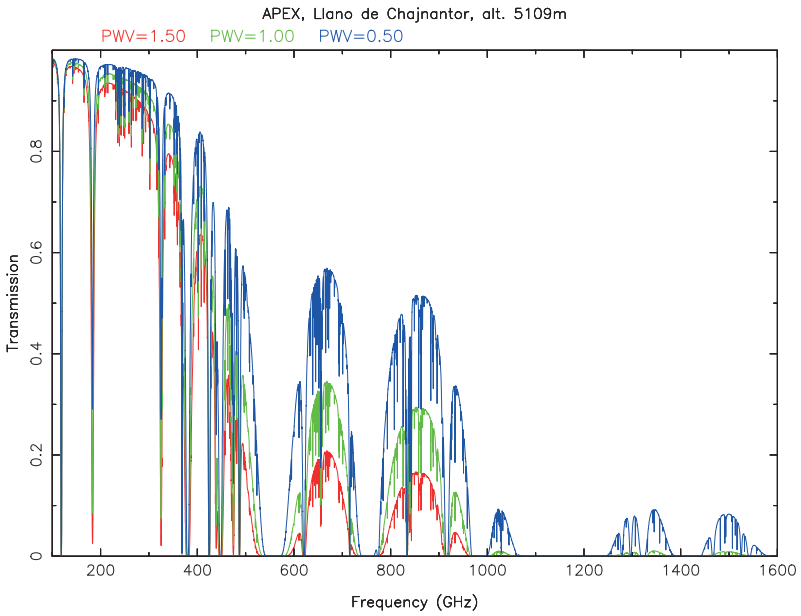

Figure 1.2: The atmospheric transmission[13] at the APEX site in Chile at an altitude of 5109 m Llano de Chajnantor shown as a function of frequency for different pwv. The model generating the atmospheric transmission for different atmospheric conditions is based on a ATM model written by Pardo et al. (2001).

1.3.1 *Herschel* Space Observatory

General references: Pilbratt et al. (2010); de Graauw et al. (2010)

In May 2009 *Herschel* Space Observatory was launched as the first observatory to cover the entire range from far-infrared to sub-millimeter wavelengths with the largest mirror ever launched into space – 3.5 m. The goal was to explore the far-infrared band better than any previous mission with extremely sensitive in-

[10] http://www.snsb.se/en/Home/Space-Activities-in-Sweden/Satellites/Odin/
[11] http://www.esa.int/Our_Activities/Space_Science/Herschel
[13] http://www.apex-telescope.org/sites/chajnantor/atmosphere/

struments. To provide a stable thermal and radiation environment it was placed in a halo orbit around the second Lagrange point (L2). This is one of five points in space were a small body theoretically can sustain a stable orbit with respect to the Earth and the Sun. By the end of April 2013 *Herschel* ran out of helium which was the main coolant of its instruments and was decommissioned later the same year. However, *Herschel* had already collected an enormous amount of remarkable data which will take many astronomers and PhD students many years to analyze.

The spacecraft operated three advanced instruments covering different wavelength bands: two cameras and one very high-resolution spectrometer. The Photodetector Array Camera and Spectrometer (PACS) provides the user with imaging capabilities at 60–210 μm, and the Spectral and Photometric Imaging Receiver (SPIRE) uses bolometer arrays at 250, 350 and 500 μm. Both instruments were also capable to do spectroscopy, however with low resolution. Using the the third instrument, the Heterodyne Instrument for the Far Infrared (HIFI), a much higher spectral resolution could be obtained at high sensitivity due to the state-of-the-art superconducting mixers with near quantum-noise limits.

HIFI covered the frequency ranges $480 - 1250$ GHz ($625 - 240$ μm) and $1410 - 1910$ GHz ($213 - 157$ μm), split in seven different bands. In total four spectrometers were available: two Wide Band Acousto Optical Spectrometers (WBS) and two High Resolution Autocorrelation Spectrometers (HRS), one for each polarization and bandwidth, which are an excellent tool to reduce the final noise level, if the data quality allows.

Data reduction using HIPE

The Herschel Interactive Processing Environment (HIPE)[14] is the Herschel data reduction pipeline software, designed to produce calibrated dataproducts which can either be analyzed in that environment or exported to other preferred formats. For further details on data reduction of *Herschel*-HIFI data see appended Paper II.

[14] `http://herschel.esac.esa.int/HIPE_download.shtml`

Chapter 2

Star formation

General references: Stahler & Palla (2005) ; Hartmann (2009); McKee & Ostriker (2007)

The stellar nurseries – cold and dense molecular clouds – in the Milky Way are observed to be distributed near the plane of the disk along the spiral arms, and concentrated to the inner regions of the Galaxy in the so called "molecular ring" at a distance of about $3-5$ kpc[1] from the Galactic centre[2]. Here we find the most massive and luminous star forming regions in the Galaxy. The sizes and masses of Galactic molecular clouds span from giant star forming cloud complexes of masses[3] $\sim 10^6$ $M_\odot$ and sizes ~ 100 pc, to clouds of $\lesssim 10$ $M_\odot$ and $\lesssim 1$ pc (Dame et al., 2001, and references therein).

Star formation is traditionally divided into two parts: low-mass and high-mass star formation since their evolutionary sequences are fundamentally different. The limiting mass that separates low-mass from high-mass stars is ~ 8 $M_\odot$ and their different evolutionary scenarios are presented in Sect. 2.1 and 2.2, respectively. Our detailed understanding of star formation is, however, biased towards low-density regions with relatively low star formation rates since most observational studies have been made towards regions in the proximity of our Sun. Here the surface density of the ISM is lower than in the molecular ring and low-mass cores arise more frequently than massive ones. Since most massive stars are located at large distances in the molecular ring they are also difficult to resolve, as most single dish radio telescopes give far too low spatial resolution. The details of the formation of massive stars and the corresponding mass accretion is thus still not very well understood. The spectacular new interferometer telescope ALMA. ALMA is located in the Atacama desert, Chile, at an altitude of 5000 m. This

[1] pc is short for parsec, which corresponds to a distance of 3.26 light years or 0.2 million au.

[2] Our Sun is located ~ 8.3 kpc (Reid et al., 2014) from the Galactic center.

[3] The mass of our Sun, $M_\odot$, is the unit used in astronomy to indicate the masses of e.g. stars, nebulae and galaxies.

antenna is revolutionary in terms of sensitivity and spatial resolution and will when completed consist of 66 high precision antennas. The first observations started already in September 2011, using part of the array, and the official inauguration took place in March 2013. (Atacama Large Millimeter Array) promises a revolution in the field of star formation and will provide detailed imaging of local star and planet formation in the coming years.

2.1 Low-mass stars

Star formation theories are based on a few key physical processes and timescales: *(i)* Gravitational collapse which involves both the *balance between gravity and pressure*, as well as *(ii) cooling* processes, and *(iii)* the *time scales* for cloud collapse, gas accretion to a torus of matter orbiting the proto-star and to the proto-star itself, and finally for a star to contract before its nuclear fusion starts. These processes are discussed below, as well as the importance of their relative time-scales.

2.1.1 Gravitational collapse

To understand what the necessary physical conditions are for a gravitational collapse to occur, the effects that small perturbations have on a system in hydrostatic equilibrium can be considered. Although several simplifying assumptions are made, such as neglecting external pressure, effects due to rotation, turbulence, and galactic magnetic fields, the below analysis provide valuable insights on the most important processes in star formation.

Balance between gravity and pressure

The condition of equilibrium for a stable, gravitationally bound system can be described by the virial theorem

$$2\,K + U = 0\ , \tag{2.1}$$

where K is the kinetic energy and U is the potential energy[4]. If the kinetic energy is higher than half the absolute value of the potential energy, then the force due to gas pressure will dominate over the inward directed force of gravity. But if the internal kinetic energy is lower, then the cloud will collapse. The condition for collapse implied by the virial theorem, $2K < |U|$, can be used to find an expression for the minimum radius, $\lambda_{\rm c}$, and mass, $M_{\rm c}$, necessary to initiate spontaneous gravitational collapse of a cloud.

[4]Implicitly assumed to be averaged over time.

Assuming a spherically symmetric cloud of constant density, the gravitational potential energy is approximately

$$U \sim -\frac{3}{5}\frac{G\,M_c^2}{\lambda_c} , \tag{2.2}$$

where G is the gravitational constant. When microscopic thermal energy dominates, the total kinetic energy of the cloud is

$$K = \frac{3}{2} N\,k_{\rm B}\,T_{\rm K} , \tag{2.3}$$

where $k_{\rm B}$ is the Boltzmann constant, $T_{\rm K}$ is the gas kinetic temperature and N is the total number of particles, also written as

$$N = \frac{M_{\rm c}}{\mu\,m_{\rm H}} , \tag{2.4}$$

where μ is the mean molecular weight (the average mass of a free particle in the gas in units of the mass of the hydrogen atom), and $m_{\rm H}$ is the hydrogen mass. The condition for collapse implied by the virial theorem, $2K < |U|$ becomes

$$\frac{3\,M_c\,k\,T_{\rm K}}{\mu\,m_{\rm H}} < \frac{3}{5}\frac{G\,M_c^2}{\lambda_c} . \tag{2.5}$$

Using the initial mass density of the cloud, ρ_0, assumed to be constant throughout the cloud, the radius of the sphere can be written as

$$\lambda_c = \left(\frac{3\,M_c}{4\,\pi\,\rho_0}\right)^{-1/3} . \tag{2.6}$$

After substitution into equation (2.5) the minimum mass can be found. The boundary condition between expansion and collapse is known as the *Jeans criterion* after Sir James Jeans (1877-1946) who was one of the first to investigate this problem in the beginning of the century

$$M_{\rm c} > M_{\rm J} , \tag{2.7}$$

where

$$M_{\rm J} = \left(\frac{5\,k\,T_{\rm K}}{G\,\mu\,m_H}\right)^{\frac{3}{2}} \left(\frac{3}{4\,\pi\,\rho_0}\right)^{\frac{1}{2}} , \tag{2.8}$$

is called the Jeans Mass. Using equation (2.6) we can express the Jeans criterion in terms of the minimum radius necessary to collapse a cloud with density, ρ_0:

$$\lambda_{\rm c} > \lambda_{\rm J} , \tag{2.9}$$

where

$$\lambda_{\rm J} \,=\, \left(\frac{15\,k\,T_{\rm K}}{4\,\pi\,G\,\mu\,m_H\,\rho_0}\right)^{\frac{1}{2}} \,, \tag{2.10}$$

is the Jeans length.

Defining the particle number density in units of cm^{-3}, $n = \rho_0/(\mu\, m_{\rm H})$, and using a mean molecular weight of 2.36[5], the Jeans mass of equation (2.8) can be expressed as a function of kinetic temperature and number density,

$$M_{\rm J} \,\sim\, 540\,\left(\frac{T_{\rm K}}{10\,{\rm K}}\right)^{3/2}\, n^{-1/2}\,[{\rm M}_\odot]\,. \tag{2.11}$$

Since 99.99 % of all molecules are molecular hydrogen and since the atomic fraction is very low in the dense cores where star formation occurs, the total number density, n, is very well measured by the molecular hydrogen number density, $n_{\rm H_2}$.

Note that this result assumes a homogeneous, uniform cloud with no initial net pressure or gravitational forces. However, pressure caused by turbulence and magnetism play an important role and may increase the critical mass needed for core collapse. The dust extinction here plays an important role, reducing the radiative heating and ionization by luminous stars and consequently reducing turbulent motions. Uniform density is also not consistent with hydrostatic equilibrium which requires a pressure gradient to support the gravitational force. The relative distribution of material will also change with time during the collapse. The concept of Jeans mass can thus be viewed upon as a *lower limit* to gravitationally bound cores. However, the main criterion is that the temperature needs to be low and the density high. Otherwise the Jeans mass will increase and thereby decreasing the probability of spontaneous collapse.

For a dense core of a giant molecular cloud, typical temperatures and number densities are $T_{\rm K} = 10$ K and $n_{\rm H_2} = 10^4$ cm^{-3}. Since dense clouds are predominantly of molecular hydrogen, $\rho_0 = 2\,m_{\rm H}\,n_{\rm H_2} = 3\times10^{-10}$ g cm^{-3} and $\mu \simeq 2$. The Jeans mass becomes $M_J \sim 8$ M$_\odot$, compared with $M_J \sim 1500$ M$_\odot$ for a typical diffuse hydrogen cloud where $T = 50$ K, $n_{\rm H} = 5\times10^2$ cm^{-3}, $\rho_0 = 8\times10^{-12}$ g cm^{-3} and $\mu \simeq 1$.

The virial theorem can also be expressed in terms of the total energy of the system, $\langle E\rangle = \langle K\rangle \,+\langle U\rangle$ (mean values over a time interval which is long enough to eliminate fluctuations, but short in comparison to the time scale for the evolution of the system), namely as

$$\langle E\rangle = \frac{1}{2}\,\langle U\rangle\,. \tag{2.12}$$

This implies that the potential energy of a large cloud, which is initially zero, must change to a negative static value in order for a star to be formed by gravitational

[5]Assuming a fully molecular gas where all hydrogen is in H_2 and a 20 % helium abundance (by number) we find that the mean molecular weight, $\mu = \overline{m}/m_{\rm H}$, where $\overline{m}$ is the average mass of a gas particle, is 2.36.

collapse. During the collapse the released gravitational energy is transformed to heat which is radiated into space by the gas particles during the collapse.

Cooling

When a system is in equilibrium the inward acting gravitational force is counterbalanced by the outward internal pressure of the cloud. Only if the gravitation exceeds the pressure will a collapse occur; however, it will halt if the total outward forces once again become larger than the gravitational force. This can happen during a collapse for instance from the release of gravitational energy which increases the kinetic energy. Hence, the collapse will stop – unless the medium is able to cool.

Atoms, ions and molecules have the ability to convert the kinetic temperature of the gas through collisions to radiation which can escape from the cloud. In particular molecules through rotational transitions. This process is most efficient for temperatures between 10 and 100 K. However, the most abundant molecule, H_2, has its first rotational transition (see section 1.2.1) at an energy level equivalent to $\sim$500 K. Therefore, cooling of gas below this temperature relies on the presence of heavier species such as e.g. atomic oxygen, ionized carbon, atomic carbon, carbon monoxide and water.

When the first stars were born in the early Universe, H_2 and its deuterated form HD provided essentially all cooling, producing critical masses much higher than today. Therefore, the first stars in the Universe are expected to have been more massive ($\sim 10 - 200$ $M_\odot$) than the typical stars observed ($\lesssim 1$ $M_\odot$) today.

Timescales

To fully frame the theory of star formation several important time scales have to be considered. The first is the *free-fall time* needed for all parts of an uniform spherically symmetric cloud to collapse to its center simultaneously without any opposing pressure to counteract gravity

$$t_{\rm ff} = \sqrt{\frac{3\pi}{32\,{\rm G}\,\rho}} \sim \frac{3.4 \times 10^7}{\sqrt{n_{\rm H_2}}}[{\rm yr}]. \tag{2.13}$$

Note that this time scale is independent of the initial radius of the cloud and since all parts of the cloud will collapse with the same amount of time the density will increase at the same rate everywhere. The order of magnitude relevant for the phase of free-fall gravitational collapse is $\sim 10^5 - 10^6$ years and determines both the time scale for the formation of a star and the accretion luminosity, which is the luminosity[6] generated by a mass accretion rate, $\dot{M}$ [$M_\odot$ s^{-1}].

[6]Luminosity is a measurement of power, which describes the total rate of energy lost by a star in units of solar luminosity, $L_\odot = 3.8 \times 10^{26}$ W.

Of importance is also the *accretion time scale*

$$t_{\rm acc} = M_\star / \dot{M}_{\rm env} \ , \tag{2.14}$$

were $M_\star$ is the mass of the proto-star and $\dot{M}_{\rm env}$ is the accretion rate of matter from the envelope to the proto-star. In a simplified scenario where the latter has a constant value of $\sim 10^{-5}$ $\mathrm{M}_\odot$ yr^{-1}, the accretion time scale sets the duration of the envelope accretion phase to a few 10^5 years for a typical low-mass proto-star with mass $\lesssim 1$ $\mathrm{M}_\odot$. Note that the rate of accretion onto the circumstellar disk (a torus of matter orbiting the proto-star) can differ from the rate of accretion onto the proto-star, since some of the infalling gas can be temporarily stored in the disk.

Finally, the time it takes for the proto-star itself to contract to the point where hydrogen fusion begins has to be considered. This is governed by the *Kevin-Helmholtz time scale*

$$t_{\rm KH} = \frac{E_{\rm g}}{L_\star} = \frac{G\,M_\star^2}{R_\star L_\star}, \tag{2.15}$$

where $E_{\rm g} = G\,M_\star^2/R_\star$ is the gravitational potential energy of the proto-star, where $R_\star$ represent its radius and $L_\star$ the observed luminosity generated by gravity.

For a proto-star's location in the Hertzsprung-Russell (HR) diagram in Fig. 2.1, one can expect it to be strongly affected by accretion whenever $t_{\rm KH} > t_{\rm acc}$. For a typical low-mass stars ($t_{\rm acc} < t_{\rm KH}$), thus the accretion episode terminates before the star reaches the hydrogen burning phase. This is generally not the case for massive stars (more in section 2.2). Nevertheless, keep in mind that for a sufficiently high accretion rate any proto-star could be classified as "low-mass", according to equation (2.15) and (2.14), which is the effect of simplifying the physics of star formation.

2.1.2 Evolutionary sequence

The observations and theoretical studies performed during many years have converged on an evolutionary scenario for stars with masses up to a few $\mathrm{M}_\odot$ as outlined by Shu et al. (1987, Fig. 2.2) even though many details are still not solved. Inside filamentary over-densities ($n \gtrsim 10^3$ cm^{-3}) of several pc in size, pre-stellar cores may form with sizes of $\sim$0.1 pc, masses of several $\mathrm{M}_\odot$, densities of $\sim 10^4 - 10^5$ cm^{-3} and temperatures of ~ 10 K. The formation of a core takes place when the molecular cloud starts to fragment and slowly contract when the gravity overcomes the resisting forces of thermal gas pressure, turbulent motions, and magnetic fields. When it reaches the Jeans mass, a cloud core will then become gravitationally bound with initial conditions for a gravitational collapse. In this collapse phase a part of the core becomes optically thick and forms a "pressure-supported embryo" with initial mass of the order of 10^{-3} $\mathrm{M}_\odot$. A simplified picture is an isothermal, spherically symmetric cloud having an inside-out collapse where the inner parts collapse on a

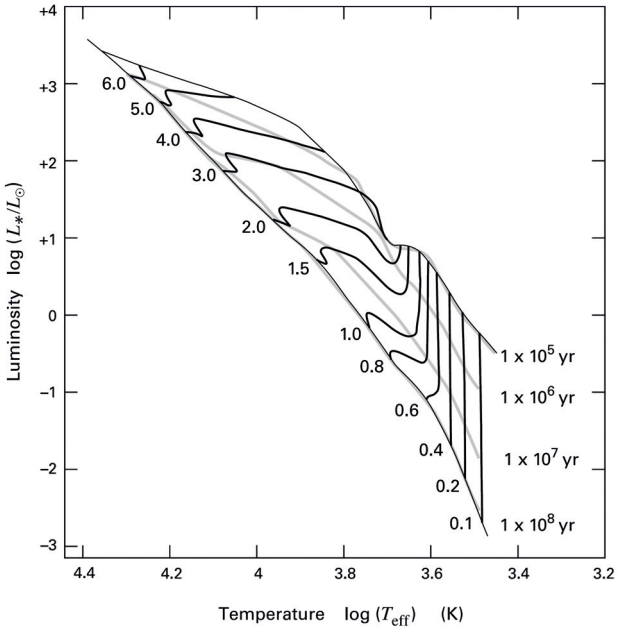

Figure 2.1: The Herzsprung-Russell diagram showing the Hyashi tracks. Credit: Stahler & Palla (2005)

shorter time-scale than the other parts. The angular momentum of the collapsing core directs the accreting gas to fall onto a rotating accretion disk formed around the proto-star. Note that this process can be an even more important factor than the heating of the gas during the contraction in stopping a gravitational collapse. The infalling material is then transported onto the proto-star via the accretion disk. The protostellar objects now evolve towards the zero-main main sequence along the so called Hayashi tracks in the H-R diagram (see Fig. 2.1) with a luminosity still powered by the gravitational energy released by the contracting star. In this late stage a strong stellar wind sets in which sweeps away the envelope material with high velocities along the rotational axis of the system. This so-called *outflow* can be for instance traced by broad water emission lines. Once the envelope is totally dispersed a pre-main sequence star with its circumstellar disk will be visible (called a T-tauri star if the mass is $\lesssim 2$ M$_\odot$ or a Herbig Ae/Be star if the mass is $\gtrsim 2$ M$_\odot$). Low-mass proto-stars will stop accreting gas before the hydrogen burning begins (c.f. the Kevin-Helmholtz time scale above), in contrast to high-mass proto-stars. All phases described above can occur simultaneously and side-by-side in a molecular cloud.

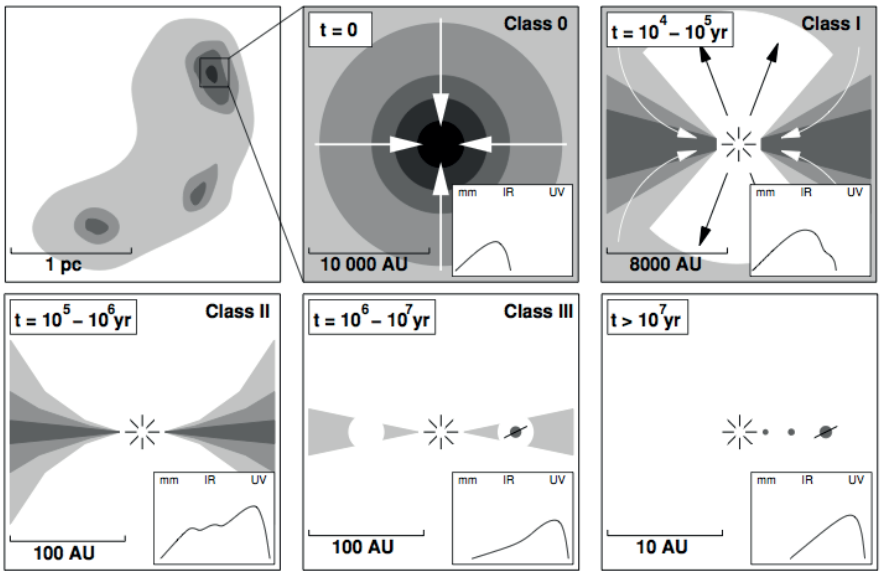

Figure 2.2: Illustration of the evolutionary sequence of young low-mass stars. Upper stages $1-3$, from left to right, 1) contracting dense molecular cores, 2) unstable cores undergoing gravitational collapse, 3) a protostar collecting material via an accretion disk surrounded by a remnant envelope. Lower stages $4-6$, from left to right, 4) an optically thick disk, 5) an optically thin debris disk with possible planet-disk interactions, 6) a main sequence star that has dispersed its entire disk where only a planetary system is left. The lower right corner shows the typical SED for the object in consideration. Credit: Jonkheid (2006), *Chemistry in evolving protoplanetary disks* (Figs. 1.1 and 1.2), based on the theory by Shu et al. (1987).

The evolutionary progression of proto-stars is traditionally divided into four classes, or stages, purely based on the slope of the spectral energy distribution (SED) in the mid-infrared regime:

- **Class 0**: sources with a central proto-star and an envelope mass larger than the former. In this embedded stage the star acquires a significant fraction of its final mass. They are extremely faint in the optical and near-infrared.
- **Class I**: sources that are believed to have relatively evolved proto-stars with both circumstellar disks and envelopes. The proto-star's SED peaks at infrared wavelengths.
- **Class II**: probably pre-main sequence stars with significant circumstellar

disks, where the envelope has been cleared away by the pre-stellar wind. The star's SED is flat at infrared wavelengths with a sharp cut-off to millimeter wavelengths.

- **Class III**: pre-main sequence stars that are no longer accreting significant amounts of matter. The star's SED shows a steady shallow decline from infrared to millimeter wavelengths.

However, this classification should be applied with caution, since it is well-recognized that the geometry of an observed source can confuse the classification scheme. A given source may appear as a Class II source at small or moderate inclination angles with a visible central source, or as a Class I source at large inclination angles when the central source is obscured by the disk.

2.2 High-mass stars

General references: Zinnecker & Yorke (2007); Bonnell et al. (1998); Crowther et al. (2010)

Approximately one percent of the stars in our galaxy live fast and die young. This dramatic way of living depends on where and under what circumstances these stars form. Their high luminosities (more than $\gtrsim 10^4$–10^6 $L_\odot$) dominate the appearance of star forming galaxies, but also result in lifetimes of only a few tens of 10^6 years compared to the 10^{10} years for a solar-type main sequence star. A core-collapse supernova, gamma-ray burst (GRB) or a direct collapse to a black hole are the evolutionary fates of these ~ 8–150 $M_\odot$ stars. They distinguish themselves from their less glamorous but more common cousins – the death of low-mass stars simply ends with slowly fading away as white dwarfs. The death rate of massive stars has been shown to be closely correlated to the stellar birth rate as they have the potential to both disrupt their natal molecular cloud and trigger further star formation.

Massive stars are typically seen to be concentrated in the centers of star clusters, inside giant molecular clouds typically located close to the galactic centre. The number of low-mass stars observed to form in low- vs. high-mass clusters are very similar, although massive stars are restricted to massive clusters. The comparison between clusters of different masses in Table 2.1 shows that a low-mass cluster typically has no massive stars while more massive clusters, e.g. the Orion nebula or NGC3603, have stars with masses $\gtrsim 40$ $M_\odot$. The most massive star found until recently, has an upper limit of 320 $M_\odot$. The star is named R136a1 and is located within the massive young stellar grouping R136 with an age of only a few million years residing in the 30 Doradus Nebula – a turbulent star forming region in the Large Magellanic Cloud (LMC), a satellite galaxy of our Milky Way (Crowther et al., 2010).

Table 2.1: The total and maximum observed stellar mass in different clusters in large molecular clouds in Milky Way and LMC. The most massive star found until today is located in R136 in the LMC.

Molecular cloud	Cluster mass $M_\odot$	Most massive star $M_\odot$
ρ Oph[a]	$\lesssim$100	< 8
Orion Nebula Cluster[a]	$\sim$2000	$\sim$40
NGC3603[b]	$\sim 10\,000$	$\gtrsim 100$
R136[b]	$\sim 55\,000$	~ 320

[a]Crowther (2012); [b]Crowther et al. (2010)

Spectroscopic observations have shown that high-mass stars are either early B stars (8–20 $M_\odot$) or O stars ($\geqslant 20$ $M_\odot$). However, details about their formation process remain scarce since their evolutionary time scales are short, they are typically observed at large distances, form in clusters which do not easily allow a separation of the objects, and they are also heavily obscured by dust.

The differences between the formation of high- and low-mass stars are presented in section 2.2.1 and the competing concepts to describe massive star formation are discussed in section 2.2.2.

2.2.1 Evolutionary phases

The huge and massive initial molecular cloud required to form high-mass proto-stars distinguishes it from low-mass proto-star formation. Another key difference is related to the accretion phase, where high-mass objects continue to accrete even if the hydrogen burning already has started. As long as material continues falling onto the core of a high-mass proto-star it will continue to grow in mass and evolve on the main sequence to hotter and more luminous states.

The formation process of high-mass stars is hard to observe and the embedded phases are only visible in optical wavelengths during 15 % of an OB-type stars lifetime. Mid-infrared to radio wavelength observations have, however, shown that the *embedded* phase of a massive proto-star can be divided into four groups of objects representing their evolutionary stages:

- **Infrared dark clouds** (IRDCs) are typically observed in extinction against bright mid-infrared emission of the Galactic plane (at 8 μm) or as a faint envelope of emission from cold dust at 850 μm. Each of the IRDCs contain at least one, if not multiple, compact $\leqslant 0.5$ pc dust cores with masses of $\sim 10^2 - 10^4$ $M_\odot$. Their dense ($10^2 - 10^4$ cm^{-3}) and cold ($10 - 20$ K) internal

regions are believed to have the initial conditions needed to form high-mass stars (Rathborne et al., 2006).

- **Hot molecular cores** (HMC) are internally heated and centrally dense massive molecular gas clouds with diameters of $\lesssim 0.1$ pc. Their high gas phase abundances of complex organic molecules are thought to result from evaporation of ices from the dust grains at the elevated temperatures. In addition, HMC:s are therefore signposted by methanol emission and water masers. Their strong emission lines are excited at temperatures > 100 K and densities $> 10^6$ cm^{-3} often tracing an outflow or a disk. These objects are often observed to be associated with nearby, or in some cases embedded, ultra-compact H II regions described below (Kurtz et al., 2000).

- **Hyper/ultra-compact H II regions** (HC H II or UC H II) are small but growing pockets of ionized gas that very likely represent the evolutionary stage which follows the natal environment of high-mass stars (the HMC phase). A HC H II region is believed to represent individual photoevaporating disks, while UC H II regions probably represent disk-less stars that photoionize their own cocoons and massive envelopes. UC H II regions are also known as the most luminous objects in the Galaxy at far-infrared wavelengths (Kurtz et al., 2000) (Peeters et al., 2002).

- **Compact and classical H II regions** (C H II and H II regions) are dense and globally ionized regions surrounding newly formed and still deeply embedded O and B stars. They are formed as the dense and ionized gas of UC H II regions expand in size at the expense of the molecular gas. If the expansion continues, the parent molecular cloud will be disrupted and reveal both the embedded high-mass and low-mass stellar population for optical and near-IR observations (Peeters et al., 2002).

2.2.2 Formation models

It is believed that the formation of high-mass stars up to ~ 20 M$_\odot$ may mimic that of lower mass stars. Formation of even more massive stars require alternative accretion scenarios. In recent literature three competing concepts have been suggested for these stars, where each depend on the initial and environmental conditions of the parent cloud. The models are: *(a)* Monolithic collapse and disk accretion; *(b)* Competitive accretion and runaway growth; and *(c)* Stellar collisions and mergers. The primary difference between the first two scenarios is that in *(a)* the mass is assumed to be gathered *before* the star formation process begins, whereas in *(b)* the mass is gathered *during* the star formation process.

Monolithic collapse and disk accretion

This model is like a scaled-up version of the low-mass star formation model. It is based on simulations of collapsing molecular cores of masses $\gtrsim 30$ $M_\odot$, initially isolated, rotating, and non-magnetic. In this model it is not possible to spatially distinguish between the formation of a dense central cluster, a multiple-star system or a single massive object. Therefore it only provides an upper limit to the mass of all stars that could possibly be formed for the considered case. A typical collapse simulation of a 120 $M_\odot$ molecular clump form a ~ 43 $M_\odot$ star (Yorke & Sonnhalter, 2002). And even more massive stars could conceivably be created with larger initial masses or a more focused flow of gas along a filament.

Rapid accretion through the disk – which in turn feeds the central object – provides an efficient angular momentum transfer in this model, allowing the star to become massive. This process could be possible by weak magnetic fields caused by turbulence and/or spiral density waves excited by gravitational instabilities. A environment not unusual when having nearby companions and may explain why massive stars are generally members of multiple systems. Furthermore, a competing effect between accretion and photo-evaporation in the disk will determine the final mass or even the upper mass limit of the star.

Critics of this model ask how high-mass stars could be formed in isolation and why not massive pre-stellar cores with long lifetimes have been found. One solution could be that turbulence supports a slow build-up as it halts the formation. Moreover, turbulence also induces density fluctuations and might fragment high-mass stars into a cluster of low-mass stars. This could, however, be stabilized by magnetic fields and support massive cores against sub-fragmentation.

Competitive accretion and runaway growth

This model is based on the gathering of matter by the gravitational potential of a proto-cluster clump or cluster of stars, funneling a significant fraction of gaseous material to the cluster center where it will be accreted by the proto-massive stars. If a clump is in a fortunate location it can significantly increase its growth and its gravitational attraction. However, a proto-star's ability to grow also depends on the region from which gas can be gathered. A location in the center of the cluster is certainly beneficial compared with ending up in the more widespread OB associations.

Because dense molecular gas clouds have finite mass, the protostellar masses will eventually compete for cloud gas when their accretion radii start to overlap. This process, combined with the action of the cluster to gather matter from large distances and focus it toward the accreting stars, makes competitive accretion a powerful mechanism to form high-mass stars. Despite the advantages of this model it has been criticized because the simulations start from a strongly gravitationally bound proto-cluster of clouds. Observationally such assemblies of clouds appear

to be supported by turbulent motions preventing protostellar masses to form. Nevertheless, supersonic[7] turbulence also implies that small turbulent velocity differences between proto-stars and their neighboring gas allow significant growth in stellar mass while more distant high velocity turbulent gas cannot be accreted.

Stellar Collisions and Mergers

In cluster centers with ongoing competitive accretion, stellar collisions and mergers might be unavoidable when the stellar density is high enough. For other conditions, stellar mergers are rare and only relevant for the most massive stars in the richest young clusters. This model can thus not explain how the widespread OB associations can form. A condition that must be met for massive stars to grow through mergers is that the collision time for stars to collide, $t_{\rm coll}$, must be shorter than the time scale for stellar evolution of the most massive star in the cluster ($\sim$3 Myr). This formation scenario is only realistic at the highest stellar densities ($\sim 10^8$ M$_\odot$ pc^{-3}).

[7]Supersonic speed exceeds the speed of sound.

Chapter 3

Radiative transfer

3.1 Radiative transfer equation

General references: Rohlfs & Wilson (1996) Rybicki & Lightman (1979)

The intensity of electromagnetic radiation travelling in vacuum is independent of the distance along its path from the source. If it, however, propagates through a medium the intensity can be changed. Photons from the medium can be added to the original beam of radiation towards us, or the intensity can be extinct along its way by scattering or absorption (illustrated in Fig. 3.1). The change in specific intensity at frequency ν as radiation travels through a medium is described by the radiative transfer equation.

$$\frac{\mathrm{d}I_\nu}{\mathrm{d}s} = j_\nu - \kappa_\nu(s)\, I_\nu \ , \tag{3.1}$$

where j_ν is the emission coefficient and κ_ν is the linear absorption coefficient of the medium.

To further simplify Eq. (3.1) the optical depth is defined as

$$\mathrm{d}\tau_\nu = -\kappa_\nu \,\mathrm{d}s \ ,$$

and the total optical depth is obtained by

$$\tau_\nu(s) = \int_{s_0}^{s} \kappa_\nu(s')\,\mathrm{d}s' \ . \tag{3.2}$$

where the integral is taken against the propagation path with $\tau_\nu = 0$ at the observer and $\tau_\nu = \infty$ at an infinite distance (Fig. 3.1).

A medium is said to be *optically thick* or *opaque* if $\tau_\nu \gg 1$ and *optically thin* or *transparent* if $\tau_\nu \ll 1$. In an optically thin medium a photon of frequency ν can travel through the medium with a small probability of being absorbed, whereas in

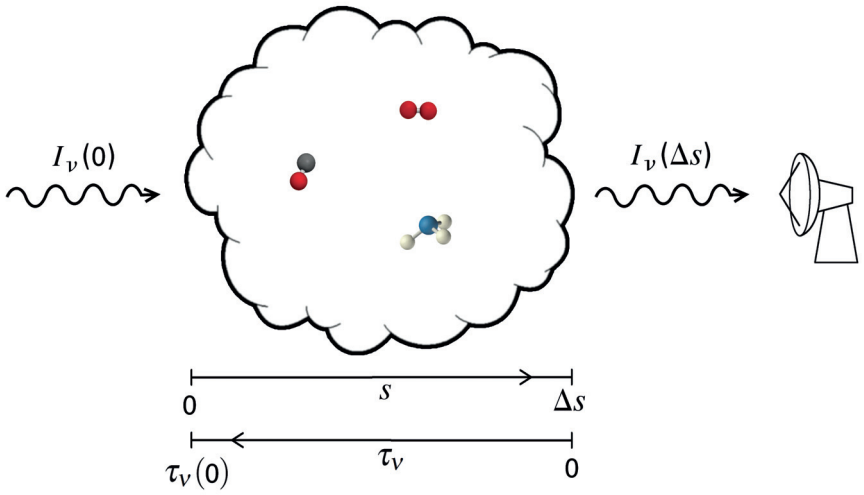

Figure 3.1: Illustration of the propagation of radiation in interstellar space along a path length s, and the optical depth. Credit: Johan Bjurström.

an optically thick medium a photon is likely to be absorbed before traversing the entire medium.

In terms of the optical depth the radiative transfer equation (3.1) can be written as

$$\frac{\mathrm{d}I_\nu}{\mathrm{d}\tau_\nu} = I_\nu - S_\nu \ , \tag{3.3}$$

where the source function, $S_\nu = j_\nu/\alpha_\nu$, describes the absorbing and emitting properties of the gas and dust particles. The dimensions for both the source function and the intensity are [erg s^{-1} cm^{-2} Hz^{-1} sr^{-1}] and these two quantities can thus be added or subtracted.

3.1.1 Solution to the radiative transfer equation

The general solution to Eq. (3.3) is

$$I_\nu(s) = I_0\, e^{-\tau_\nu(s)} + \int_0^{\tau_\nu(s)} S_\nu\, e^{-\tau_\nu+\tau'_\nu}\, \mathrm{d}\tau'_\nu \ , \tag{3.4}$$

where I_0 is the radiation contribution from the background. Assuming that the source function is constant under the integration (isothermal source) Eq. (3.4) simplifies to

$$I_\nu(s) = I_0\, e^{-\tau_\nu} + S_\nu\,(1 - \ e^{-\tau_\nu}) \ . \tag{3.5}$$

Subtracting I_0 from $I_\nu(s)$ we find

$$\Delta I_\nu(s) = I_\nu(s) - I_0 = (S_\nu - I_0)\,(1 - e^{-\tau_\nu}) \ ,$$

and it is immediately clear that the difference $S_\nu - I_0$ determines if emission or absorption will appear.

3.2 Spectral line theory

Atoms, ions and molecules can emit and absorb radiation only at distinct frequencies producing spectral lines characteristic for each species. Their excitation is governed by collisions and the radiation field.

Einstein coefficients

The Einstein coefficients describes three types of radiative transitions (see Fig. (3.2)) between quantum-mechanical energy levels, upper (u) and lower (l).

- *Spontaneous emission* from an upper to a lower state thereby emitting a photon with an energy equal to the energy level difference $\Delta E = E_\mathrm{u} - E_\mathrm{l} = h\nu_\mathrm{ul}$. The transition probability per unit time is measured by the Einstein A_ul-coefficient. It is proportional to ν_ul^3 and therefore increases strongly with frequency where a high value implies a quick decay.
- *Stimulated emission* is a second way for radiative de-excitation from an upper energy level to a lower, however, in this case the transition is induced by the presence of a photon close to the frequency of the transition. The process is described by the Einstein B_ul-coefficient and is proportional to the mean intensity of the radiation field, $\bar{J}$.
- *Stimulated absorption*, or radiative excitation. A species can absorb a photon with an energy equal to ΔE. The process is described by the Einstein B_lu-coefficient also proportional to $\bar{J}$.

The Einstein coefficients are related to each other through

$$A_\mathrm{ul} = \frac{2h\nu_\mathrm{ul}^3}{c^2} B_\mathrm{ul} \quad \text{and} \quad B_\mathrm{ul} = \frac{g_\mathrm{l}}{g_\mathrm{u}} B_\mathrm{lu} \ . \tag{3.6}$$

Boltzmann distribution

For a two energy level system, having the energy levels E_u and E_l, the ratio between the population of these levels is described by the Boltzmann distribution

$$\frac{n_\mathrm{u}}{n_\mathrm{l}} = \frac{g_\mathrm{u}}{g_\mathrm{l}}\, e^{-h\nu_{ul}/kT_\mathrm{ex}} \ , \tag{3.7}$$

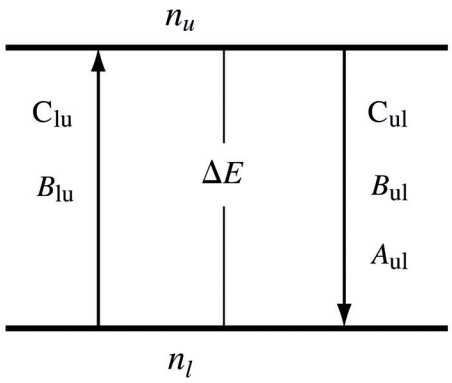

Figure 3.2: The populations in the two-level system with transition between the upper state u and the lower state l. The radiative processes are described by the Einstein coefficients.

where $g_{\rm u}$ and $g_{\rm l}$ are the statistical weights of respective level and describes the number of states with the same energy. This equation defines the excitation temperature, $T_{\rm ex}$, which is thus related to the ratio of the population of the upper and lower levels.

Collisions

For a two level system, $C_{\rm lu}$ is the number of collisional excitations and $C_{\rm ul}$ is the collisional de-excitations. The collision partners are electrons, atoms (mainly H and He) and molecules (mainly H_2). A transition from state l to state l' from a collision between an atom with for instance H_2 is described by:

$$n_l\, C_{ll'} = n_l\, n_{\rm H_2} \int_{\upsilon_0}^{\infty} \sigma_{ll'}(\upsilon)\, f(\upsilon)\, \upsilon_0 \ .$$

where n_l is the number density in state l, $n_{\rm H_2}$ is the molecular hydrogen number density, $\sigma_{ll'}$ is the collisional cross section, υ_o is defined via the threshold kinetic energy $(1/2\, m\, \upsilon_0^2)$, and $f(\upsilon)$ is the Maxwell-Boltzmann velocity distribution. This function describes the number of gas particles per unit volume having speeds between υ and $\upsilon + {\rm d}\upsilon$ by

$$f(\upsilon) = \left(\frac{m_{\rm r}}{2\pi k T_{\rm K}}\right)^{3/2} e^{-m_{\rm r}\upsilon^2/2\,k\,T_{\rm K}}\, 4\pi\upsilon^2 \ ,$$

where $m_{\rm r}$ is the reduced particle mass

$$m_{\rm r} = \frac{m_{\rm a}\, m_{\rm b}}{m_{\rm a} + m_{\rm b}} \ ,$$

and the *kinetic temperature*, T_K, is defined by

$$\frac{C_\mathrm{lu}}{C_\mathrm{ul}} = \frac{g_\mathrm{u}}{g_\mathrm{l}}\, e^{-(E_\mathrm{u}-E_\mathrm{l})/kT_\mathrm{K}} \ .$$

3.3 Types of equilibrium

Thermodynamic equilibrium (TE)

A system is in complete thermodynamic equilibrium (TE) if its particles are isolated to any influence from its environment and all processes are in perfect balance. In such system the radiation distribution is described by the Planck function

$$B_\nu(\mathrm{T}) = \frac{2h\nu^3}{c^2}\frac{1}{e^{h\nu/kT}-1} \ , \tag{3.8}$$

where h is the Planck constant and k is the Boltzmann constant. This function depends only on the thermodynamic temperature T of the environment, the gas is *thermalized* and all temperatures are the same. The intensity I_ν will not change with s hence

$$\frac{\mathrm{d}I_\nu}{\mathrm{d}s} = 0 \ ,$$

and Eq. (3.1) directly gives $I_\nu = B_\nu(T) = j_\nu/\alpha_\nu$.

Local thermodynamic equilibrium (LTE)

Full thermodynamic equilibrium will only be realized in very special conditions in a very optically thick medium. However, in an environment where the scale of the temperature variation is larger than the mean free path of particles, the matter will experience a *local thermodynamic equilibrium*. In this case the source function can still be described by $B_\nu(\mathrm{T})$, but $I_\nu \neq B_\nu$. In this environment, emission and absorption may arise.

Since $S_\nu = B_\nu$ in LTE, Eq. (3.5) can thus be written as

$$I_\nu(s) = I_0\, e^{-\tau_\nu} + B_\nu(T)\,(1 - e^{-\tau_\nu}) \ . \tag{3.9}$$

In the Rayleigh-Jeans limit, $h\nu \ll kT$, the Planck function, $B_\nu(T)$ is well approximated by

$$T_\mathrm{b} = \frac{c^2}{2k_\mathrm{B}\nu^2} I_\nu \ ,$$

where the brightness temperature, T_b, is the temperature which would result in the given brightness if inserted into the Rayleigh-Jeans law. Equation (3.9) then becomes

$$T_\mathrm{b} = T_0\, e^{-\tau_\nu} + T_\mathrm{ex}\,(1 - e^{-\tau_\nu}) \ .$$

Statistical equilibrium (SE)

In many astrophysical conditions (but not all) one can assume that the level populations are time independent, i.e. $\mathrm{d}n_\mathrm{l}/\mathrm{d}t = 0$. Hence, one can balance all upward and downward processes for each level. In a two-level system, SE can be expressed as

$$\frac{\mathrm{d}n_\mathrm{u}}{\mathrm{d}t} = -n_\mathrm{u}(A_\mathrm{ul} + B_\mathrm{ul}\overline{J} + C_\mathrm{u}) + n_\mathrm{l}(B_\mathrm{lu}\overline{J} + C_\mathrm{lu}) \equiv 0 \ , \tag{3.10}$$

$$\frac{\mathrm{d}n_\mathrm{l}}{\mathrm{d}t} = +n_\mathrm{u}(A_\mathrm{ul} + B_\mathrm{ul}\overline{J} + C_\mathrm{ul}) - n_\mathrm{l}(B_\mathrm{lu}\overline{J} + C_\mathrm{lu}) \equiv 0 \ , \tag{3.11}$$

where both equations give exactly the same result, $\overline{J}$ is the mean integrated intensity averaged over all directions μ, and all frequencies

$$\overline{J} = \frac{1}{4\pi}\int_{-\infty}^{\infty}\mathrm{d}\Omega \int I_\nu(\mu,\nu)\,\phi(\mu,\nu)\,\mathrm{d}\nu \quad , \tag{3.12}$$

where $\phi(\nu)$ is the normalised line profile

$$\phi(\nu) = \frac{1}{\sqrt{\pi}\,\nu_t}\,e^{(}-\frac{(\nu-\nu_0)^2}{\nu_t^2}) \ , \tag{3.13}$$

and ν_t is the turbulent width related to the line full width at half maximum (FWHM) as $\Delta\nu^2 = 4\ln 2\,\nu_t^2$.

The conservation of the number of particles

$$n_\mathrm{tot} = n_\mathrm{u} + n_\mathrm{l} \ ,$$

is used to replace one of Eqs. 3.10 or 3.11.

Critical density

If collisions dominate the excitation, $T_\mathrm{ex} \rightarrow T_\mathrm{K}$, and if radiative processes dominate $T_\mathrm{ex} \rightarrow T_\mathrm{rad}$. When the downward radiative processes equal the downward collisional processes the critical density, n_{crit}, is defined as

$$n_\mathrm{crit} = \frac{A_{ul}}{C_{ul}}\left(1 + \frac{1}{e^{h\nu/kT}-1}\right) \approx \frac{A_{ul}}{C_{ul}} \ .$$

The last approximation holds if $h\nu \gg kT_\mathrm{ex}$ and is widely used as a first approximation of n_crit.

3.4 The Accelerated Lambda Iteration method

To determine the contribution from spectral line emission and absorption of matter given certain physical conditions, a system of non-linear coupled equations has to be solved, which is non-trivial and time-consuming. Instead, several different methods exist to decouple these equations.

The Accelerated Lambda Iteration (ALI) is a powerful technique and is based on the method in Rybicki & Hummer (1991, 1992). The code used in Paper II was developed by Per Bergman at Onsala space observatory to solve the radiative transfer problem in a spherically symmetric geometry. With this non-LTE code, models of radiation dominated objects can be constructed with an accurate modeling of the observed molecule line emission and overlapping absorption profiles. The benchmarking of the code was done by Maercker et al. (2008). The review of the ALI method in Hubeny (2003) concluded that ALI performs as well as other radiative transfer codes and methods to reproduce line profiles.

Generalizing the SE equations to a multi-level case, one can solve the coupled problem of radiative transfer and statistical equilibrium from an initial guess of the level populations, n_i. The mean integrated intensity, $\bar{J}$, is then calculated from equation (3.12), at every radial position in the sphere and integrated over all directions and frequencies, including the background contribution from dust and emission lines overlapping the source function. The procedure is repeated with new calculations of the populations until convergence is reached.

Similar to other radiative transfer codes, ALI requires accurate knowledge of collisional rate coefficients, which can for instance be downloaded from the LAMDA[1] data base (Schoeier et al., 2005) or from BASECOL[2]. In Paper II we used collisional rate coefficients for collisions with ortho and para ammonia molecules by Danby et al.(1988). More details about the modeling and a figure of the modeled geometry is found in Paper II (Sect. 5 and Fig. 7).

Figure 3.3 shows the resulting excitation temperature ($T_{\rm ex}$) of NH_3 ($1_0 - 0_0$) as a function of the number density of molecular hydrogen, $n_{\rm H_2}$, in a spherically symmetric cloud. The radiative transfer through the cloud is solved by ALI for a constant column density, $N_{\rm H_2} = 10^{-9}$ cm^{-2}, and kinetic temperature $T_{\rm K} = 100$ K. The only heating source is the cosmic background radiation, at 2.73 K. For low $n_{\rm H_2}$ the dominant radiation field comes from radiative processes (stimulated or spontaneous emission/absorption). As the density increases, the molecules also become excited by collisions. When the density becomes high enough to dominate the radiation field, the excitation temperature becomes equal to the kinetic temperature, see discussion on critical density in the previous section.

[1] `http://www.strw.leidenuniv.nl/~moldata`
[2] `http://basecol.obspm.fr`

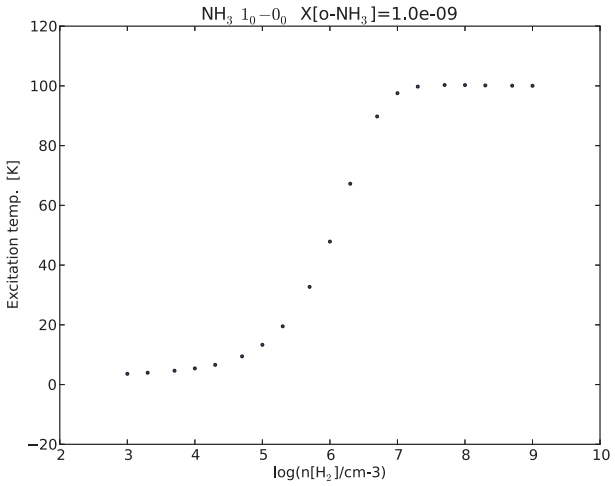

Figure 3.3: The excitation temperature ($T_{\rm ex}$) increases with the number density of hydrogen ($n_{\rm H_2}$) in a spherically symmetric cloud as modeled with ALI. Credit: Per Bergman.

3.5 Column density

The column density (defined in Eq. (1.2)) is, along with the temperature and density, a particularly interesting parameter when studying the ISM. It can be derived in several ways, but the simplest way is by expressing the absorption coefficient in terms of the Einstein coefficients as

$$\kappa_\nu = \frac{h\nu_{\rm ul}}{4\,\pi}\left(n_{\rm l}\,B_{\rm lu} - n_{\rm u}\,B_{\rm ul}\right)\,\phi_\nu\ . \tag{3.14}$$

By using the relations between the Einstein coefficients (3.6) and the Boltzmann distribution (3.7), we can re-write Eq. (3.14) to find the column density found in the lower level traced by absorption lines as

$$\begin{aligned}
\kappa_\nu\,{\rm d}s &= \frac{h\nu_{\rm ul}}{4\pi}\left(n_{\rm l}\,B_{\rm lu} - n_{\rm u}\,\frac{g_{\rm l}}{g_{\rm u}}\,B_{\rm lu}\right)\,\phi_\nu\,{\rm d}s \\
&= \frac{h\nu_{\rm ul}}{4\pi}\left(n_{\rm l} - n_{\rm l}\,e^{-\,h\nu_{\rm ul}/kT_{\rm ex}}\right)\,B_{\rm lu}\,\phi_\nu\,{\rm d}s \\
&= \frac{h\nu_{\rm ul}}{4\pi}n_{\rm l}\,\left(1 - e^{-\,h\nu_{\rm ul}/kT_{\rm ex}}\right)\,\frac{c^2}{2h\nu_{\rm ul}^3}\,\frac{g_{\rm u}}{g_{\rm l}}\,A_{\rm ul}\,\phi_\nu\,{\rm d}s \\
&= \frac{c^2}{8\pi\,\nu_{\rm ul}^2}\,\frac{g_{\rm u}}{g_{\rm l}}\,n_{\rm l}\ A_{ul}\left(1 - e^{-\,h\nu_{\rm ul}/kT_{\rm ex}}\right)\,\phi_\nu\,{\rm d}s\ .
\end{aligned} \tag{3.15}$$

where $\phi(\nu)$ is the normalised line profile (3.13).

Re-scaling from frequencies to equivalent Doppler velocities via the substitution $\mathrm{d}\nu = \nu/c\ \mathrm{d}\upsilon$, and integrating over the line profile and along the line of sight, we obtain an expression for the column density in the lower state

$$N_{\mathrm{l}} = \frac{8\pi\nu_{\mathrm{ul}}^3}{c^3}\,\frac{g_{\mathrm{l}}}{g_{\mathrm{u}}}\frac{\int \tau_\nu\,\mathrm{d}\upsilon}{A_{\mathrm{ul}}}\,\frac{1}{1-e^{-h\nu_{\mathrm{ul}}/kT_{\mathrm{ex}}}} \approx \frac{8\pi\nu_{\mathrm{ul}}^3}{c^3}\,\frac{g_{\mathrm{l}}}{g_{\mathrm{u}}}\frac{\int \tau_\nu\,\mathrm{d}\upsilon}{A_{\mathrm{ul}}}\ , \tag{3.16}$$

where the last approximation is valid when $T_{\mathrm{ex}} \ll h\nu_{\mathrm{ul}}/k$.

Absorption lines are often observed towards cold and diffuse ISM where the excitation through radiation and collisions are negligible. In such gas the only populated state will be the ground state and thus N_{l} is a very good approximation of the total column density, N_{tot}. However, if absorption lines are observed towards a dense and warm cloud (as in Paper II), higher energy states will be populated. In this case the total column will be the sum of N_{l} in all populated states

$$N_{\mathrm{tot}} = \sum N_{\mathrm{l}}\ . \tag{3.17}$$

Chapter 4

Introduction to appended papers

As mentioned in Sect. 1.3.1, *Herschel* and its sensitive HIFI instrument made it possible to observe interstellar light hydrides, which have their lowest rotational transitions at THz frequencies. These types of molecules have been studied in both papers included in this thesis, Paper I and Paper II, but for different purposes. Paper I explores the nitrogen chemistry by searching for the so far undetected NH^+ ion – a key diagnostic in the nitrogen chemistry – together with the NH_2^- anion in interstellar gas. Neither species were detected but the derived low upper limits were used to constrain chemical models. In Paper II we use the ammonia (NH_3) molecule to probe different layers of a massive star forming region in order to understand how massive stars are formed within.

4.1 Paper I

NH^+ has been theorized to exist in interstellar space for decades but searches are difficult, not only due to the expected low abundance, but also since its strongest transitions lie at frequencies impossible to observe with ground-based telescopes. Our *Herschel*-HIFI deep searches for NH^+ are the most sensitive to date, and our searches for NH_2^- was the first of its kind.

Since these species most likely will have very weak emission lines, if any, we utilize the technique of searching for absorption in sight-lines toward bright infrared sources providing strong background continuum. For this purpose we have chosen two very well-known and extremely luminous sub-millimeter and infrared star forming regions: G10.6−0.4 (W31C) and Sgr B2 (M). Figure 4.1, show a sketch of our Galaxy, the Milky Way, with several well studied strong continuum sources marked - including our sources at distances of 5 and 8.5 kpc from the Sun, respectively.

In order to claim a detection of a new species in space, several transitions, with the correct anticipated line strengths, must be detected. We therefore searched for two NH^+ fine structure transitions $N = 1-1$ $J = 1.5-0.5$ at 1 013 and 1 019 GHz.

However, hyperfine interactions, including the ^{14}N nuclear spin, split each transition into numerous hyperfine structure (hfs) components. Thus both lines have 14 hfs components each, spread over velocity ranges of 26 and 134 km s^{-1}, respectively. If the spectral resolution is high enough to resolve all components, then a detection would be rather secure even with only one detected transition. Such high resolution is not possible to use in our searches since the integration time linearly increases with resolution. In addition, the highest resolution spectrometer available using *Herschel*-HIFI covers a bandwidth too narrow for our searches. And, also the numerous emission lines from the sources themselves, in particular Sgr B2 (M), prevent detection of all individual hfs components.

Because the formation and destruction of a type of molecule depend on its environment, the abundance of a species can be used to explore the physical and chemical conditions within the observed cloud type. Even a non-detection can in this respect be a useful constraint to chemical models. In Paper I different chemical pathways of the nitrogen chemistry are explored in the different types of clouds present in our observed lines of sight.

My contribution to this paper is the challenging data-reduction. Since the *Herschel*-HIFI intrinsically is a dual sideband instrument two different methods were used to determine the sideband origin of the lines. Toward G10.6−0.4 we used three different settings of the local oscillator (LO). A spectral line will then appear at the same frequency if its origin is in the signal band. If not, the line will move across the band. This procedure, however, requires few or no emission lines from the source in the image sideband. Thus, toward Sgr B2 (M) we had to include eight different LO settings to allowed a full deconvolution of both sidebands. However, this procedure can easily introduce artifacts in the spectrum and must be treated with care. Also, when integrating to very low noise levels all small ripples and variations in the baseline become increasingly important. A lot of time was devoted to test different methods to remove standing waves and ripples.

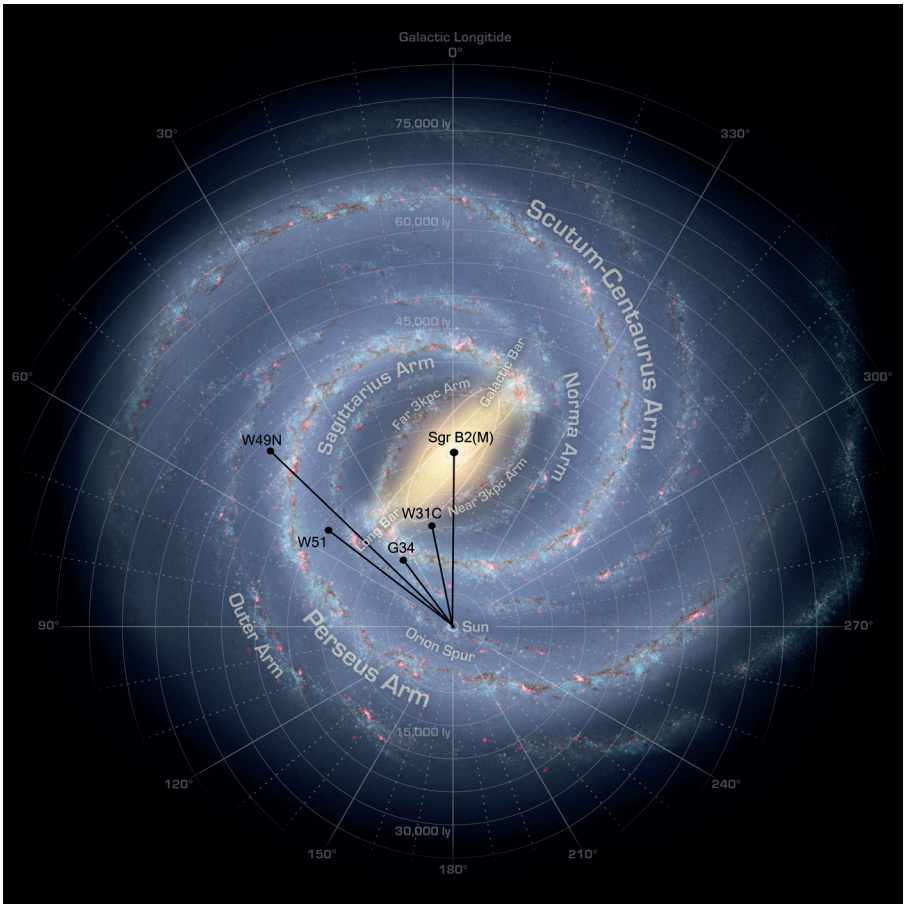

Figure 4.1: A sketch of our Galaxy, the Milky Way, adopted from NASA-JPL. The locations of five well-studied strong continuum sources are marked relative to the Sun, namely Sgr B2 (M), W49N, W31C, W51 and G34.

4.2 Paper II

In Paper II seven ammonia rotational transitions at THz frequencies were used to probe the gas accretion in the massive star forming region G34.26+0.15 (G34), located at a distance of 3.3 kpc (Fig. 4.1) in the Galactic plane.

This highly compact molecular cloud has been extensively studied in radio continuum and radio recombination lines. The radio continuum exhibit two UC H II regions (A and B), a more evolved H II region with a cometary shape (component C), and an extended ring-like H II region with a diameter of $1'$ (component D). By studying the dynamics of the gas enveloping a developed UC H II region with embedded proto-clusters of stars, evidence may be found whether accretion is still feeding the stars or not. The accretion process is directly linked to the velocity of gas clouds moving inwards toward the densest and central regions, and also to the outward radiation pressure from the star-forming clusters, as described in Sect. 2. A gas clump can become accreted by the cluster of proto-stars only if the accretion rate is higher than the outwards directed radiation pressure from the luminous proto-stars. This process is thus exposed by high inward velocities.

Pure rotational ammonia transitions at THz frequencies are useful tools to probe the dynamics of a collapsing gas cloud. A direct evidence of gas moving inwards toward a central source can be found through detailed observations of spectral line profiles. If an observed spectral line shows the signature of an inverse P-Cygni profile – emission at the source systemic velocity and a redshifted absorption component – this is usually interpreted as infalling gas. Using the HIFI instrument onboard the *Herschel* space observatory we were able to detect not only both ortho- and para-symmetries of the fundamental rotational transitions, but also lines from higher energy states. The characteristic P-Cygni profile was seen in all the detected ammonia transitions toward G34, even though the highest exited transitions showed very little emission. The advantage with observations toward a bright far infrared continuum is the possibility of absorption at any velocity. In this case, spectral lines may absorb radiation not only close to the source velocity, but also from infalling gas at much higher velocities than covered by the emission line which otherwise acts as the only continuum possible to absorb. This is also clearly seen in our detected ammonia line profiles where the absorption is detected at increasingly higher velocities for higher excited transitions. These lines therefore probe different layers of the dense molecular cloud. A closer analysis of the line profiles suggested that this velocity shift with energy levels was not continuous but seemingly arising from two separate gas components moving inward towards the central region, each with a constant velocity.

In order to investigate the possible accretion scenario suggested by the line profiles, a radiative transfer code had to be utilized since the ammonia emission and absorption lines are produced in conditions far from equilibrium. The radiative transfer code ALI, described in Sect. 3.4, was used to model the G34 molecular

cloud and star forming region as a spherically symmetric, dense molecular cloud with a centrally heating source. The sphere is modeled with a number of shells, each having a constant velocity where the inward velocity, temperature and density increases toward the center. Further details on the model are found in Paper II.

The detailed ALI modelling of the the observed ammonia absorption line profiles confirmed the existence of two gas clouds moving towards the central region of G34 with high enough velocities to be accreted by the forming high-mass proto-stars. This observational evidence supports the competitive accretion model, described in detail in Sect. 2.2.2.

4.2.1 Future work

The set of ammonia rotational transitions observed and used in the analysis of G34 has also been observed towards three additional Galactic massive star forming regions: G10.6−0.4 (W31C), W49N and W51, all marked in Fig. 4.1. Therefore, in a similar way as for G34, I will do the data-reduction, analysis, and spectral line profile modeling in ALI of the observations towards each of these three sources. As a result, we may compare the sources to each other as each region may represent a different evolutionary phase of high-mass star formation.

Bibliography

Bonnell, I. A., Bate, M. R., & Zinnecker, H. 1998, MNRAS, 298, 93

Buhl, D. & Snyder, L. E. 1970, Nature, 228, 267

Cheung, A. C., Rank, D. M., Townes, C. H., Thornton, D. D., & Welch, W. J. 1968, Physical Review Letters, 21, 1701

Crowther, P. 2012, Astronomy and Geophysics, 53, 040000

Crowther, P. A., Schnurr, O., Hirschi, R., et al. 2010, MNRAS, 408, 731

Dame, T. M., Hartmann, D., & Thaddeus, P. 2001, ApJ, 547, 792

de Graauw, T., Helmich, F. P., Phillips, T. G., et al. 2010, A&A., 518, L6

Hartmann, L. 2009, Accretion Processes in Star Formation: Second Edition (Cambridge University Press)

Hartquist, T. W. & Williams, D. A. 1995, The Chemically Controlled Cosmos (Cambridge, UK: Cambridge University Press)

Hubeny, I. 2003, in Astronomical Society of the Pacific Conference Series, Vol. 288, Stellar Atmosphere Modeling, ed. I. Hubeny, D. Mihalas, & K. Werner, 17

Jonkheid, B. J. 2006, PhD thesis, Leiden Observatory, Leiden University, P.O. Box 9513, 2300 RA Leiden, The Netherlands

Klemperer, W. 1970, Nature, 227, 1230

Kurtz, S., Cesaroni, R., Churchwell, E., Hofner, P., & Walmsley, C. M. 2000, Protostars and Planets IV, 299

Maercker, M., Schöier, F. L., Olofsson, H., Bergman, P., & Ramstedt, S. 2008, A&A., 479, 779

McKee, C. F. & Ostriker, E. C. 2007, Ann. Rev. Astron. Astrophys., 45, 565

Pardo, J. R., Cernicharo, J., & Serabyn, E. 2001, IEEE Transactions on Antennas and Propagation, 49, 1683

Peeters, E., Martín-Hernández, N. L., Damour, F., et al. 2002, A&A., 381, 571

Pilbratt, G. L., Riedinger, J. R., Passvogel, T., et al. 2010, A&A., 518, L1

Rathborne, J. M., Jackson, J. M., & Simon, R. 2006, ApJ, 641, 389

Reid, M. J., Menten, K. M., Brunthaler, A., et al. 2014, ApJ, 783, 130

Rohlfs, K. & Wilson, T. L. 1996, Tools of Radio Astronomy

Rybicki, G. B. & Hummer, D. G. 1991, A&A., 245, 171

Rybicki, G. B. & Hummer, D. G. 1992, A&A., 262, 209

Rybicki, G. B. & Lightman, A. P. 1979, Radiative processes in astrophysics (Wiley-Interscience)

Schoeier, F. L., van der Tak, F. F. S., van Dishoeck, E. F., & Black, J. H. 2005, VizieR Online Data Catalog, 343, 20369

Snow, T. P. & McCall, B. J. 2006, Ann. Rev. Astron. Astrophys., 44, 367

Stahler, S. W. & Palla, F. 2005, The Formation of Stars (Wiley-VCH)

Tielens, A. G. G. M. 2010, The Physics and Chemistry of the Interstellar Medium (Cambridge, UK: Cambridge University Press)

Woods, R. C., Dixon, T. A., Saykally, R. J., & Szanto, P. G. 1975, Physical Review Letters, 35, 1269

Yorke, H. W. & Sonnhalter, C. 2002, ApJ, 569, 846

Zinnecker, H. & Yorke, H. W. 2007, Ann. Rev. Astron. Astrophys., 45, 481

struction, radiative and collisional excitation, and reactive interchange processes in interstellar space. From statistical considerations the ammonia OPR is expected to have the high temperature equilibrium value of unity if formed in the gas-phase by highly exoergic processes. In contrast, if ammonia is produced on cold dust grains then the OPR of the desorbed ammonia is expected to be higher than unity since the lowest ortho level is 22 K below the lowest para level and no rapid allowed radiative and non-reactive collisional transitions exist that can change the spin orientations between the two symmetries once formed. Therefore, a measure of the OPR and the so called spin temperature have been considered to reflect the formation temperature and pathways.

Measurements of the ortho $1_0 - 0_0$ and $2_{1,-} - 1_{1,+}$ para lines with *Herschel*-HIFI in the diffuse interstellar gas toward two star-forming regions, W31C and W49N, have, however, unexpectidly resulted in an OPR *below* unity, $\sim 0.5 - 0.7$ (Persson et al. 2012). This has recently been explained as a result of a low-temperature para-H_2 enriched gas that naturally drives the OPR of nitrogen hydrides to values below unity which otherwise have been considered as impossible since no radiative transitions are allowed between ortho and para states (Faure et al. 2013).

Our new observations and analysis of three ortho and three para lines probing different energies can for the first time be used to estimate the OPR in dense and warm gas in star-forming regions. Using the results from Table 3 we find

$$N(\mathrm{ortho}) \gtrsim \sum N_{\mathrm{l}}(\mathrm{ortho}) = 6.0 \times 10^{13} \ \ [\mathrm{cm}^{-2}] \, ,$$

and

$$N(\mathrm{para}) \gtrsim \sum N_{\mathrm{l}}(\mathrm{para}) = 1.6 \times 10^{14} \ \ [\mathrm{cm}^{-2}] \, ,$$

that gives us an OPR~0.4 in the absorbing material, below unity in agreement with Persson et al. (2012) but lower than found by Faure et al. (2013). This result takes into account all $J \leqslant 3$ and $K \leqslant 2$, but not the $J = 4 \leftarrow 3$ levels which may be populated. It is, however, not likely that the addition of these levels would increase the OPR substantially, and therefore the indication of an OPR less than unity is quite secure.

5. Spherical non-LTE modeling

The ammonia line profiles exhibit a mixture of emission and absorption in the presence of a strong submm-wave continuum. Such spectra suggest that the radiating envelope is stratified and that it contains gaseous molecules like NH_3 mixed with dust. The continuum radiation is intense; for example, $T_{\mathrm{b}} = 5$ K at 1215 GHz corresponds to a surface brightness $I_\nu = 2.7{\times}10^{-15}$ W m^{-2} Hz^{-1} sr^{-1} averaged over the 17″ *Herschel* beam. This means that the absorption rate in the $2_{1+} \leftarrow 1_{1-}$ transition is

$$I_\nu B_{\ell,\mathrm{u}} = 1.9 \times 10^{-3} \ \ \mathrm{s}^{-1} \, ,$$

where $B_{\ell,\mathrm{u}}$ is the Einstein coefficient for absorption. In comparison with the rate coefficient for collisional excitation in the same transition at collision temperature of 50 K, $C_{21} = 4.0 \times 10^{-11}$ cm^3 s^{-1} (Danby et al. 1988), a hydrogen density of $n(\mathrm{H_2}) = 4.8 \times 10^8$ cm^{-3} would be required for collisions to compete with radiative processes (cf. the critical density for emission in Table 2). Consequently, the excitation of NH_3 is probably not in local thermodynamic equilibrium (LTE). Such spectra thus require analysis by means of a non-LTE radiative transfer model of a dynamical envelope.

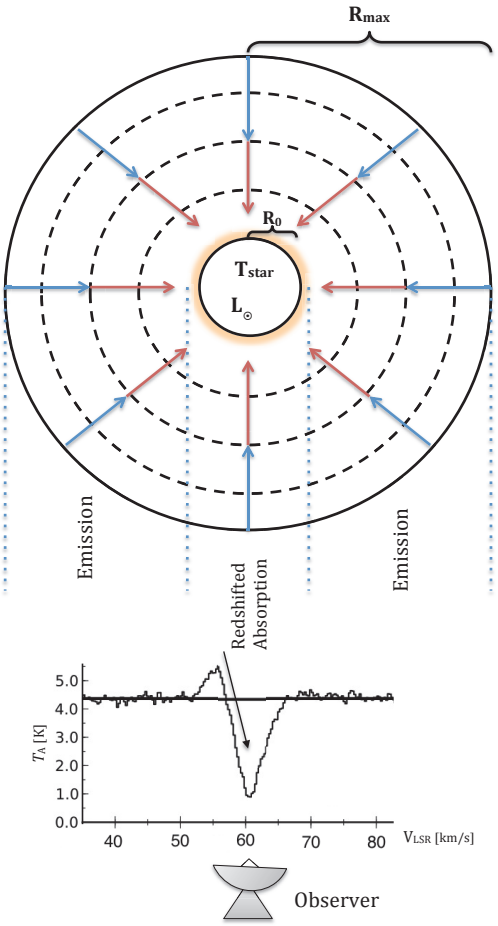

Fig. 7: Sketch illustrating the spherical ALI model with shells, an inner source, and two velocity fields in the contracting envelope. The absorption feature is due to the redshifted part of the envelope in front of the strong continuum from the H II region and the hot dust through out the gas cloud.

In order to accurately model and properly taking continuum and overlapping into account between the observed NH_3 line emission and absorption profile, we adopt a non-LTE, one-dimensional, radiative transfer model based on the accelerated lambda iteration (ALI, Rybicki & Hummer 1991, 1992) method. ALI solves the coupled problem of radiative transfer and statistical equilibrium from an initial guess of the level populations.

5.1. Method

The source is modeled as a sphere where physical properties like density and temperature can be varied over a number of homogeneous shells to reproduce radial profiles as obtained from e.g. continuum observations. The number of shell-like cells and angles used in the ray-tracing can be arbitrarily chosen. Figure 7 shows an illustration of the model and how the inverse

P-Cygni line profile is produced. In the present work, typically 20 shells and 16 angles are used. The background continuum radiation (mainly from the star-forming cluster) has a large influence on both line shapes and intensities and is modeled for each shell. The non-LTE ALI code we employed has been used in e.g. Wirström et al. (2010), Bjerkeli et al. (2011), and benchmarked by Maercker et al. (2008) where the ALI technique is described in more detail.

The foremost advantage of ALI is non-LTE modeling through the entire cloud, and that we can set profiles for the parameters producing the emission and absorption line profiles as well as continuum levels which, convolved to the corresponding beam size, can be compared to our observations. As a result we also obtain information of the opacities and excitation temperatures as a function of radius.

Radiation

The radiation field consists of the infrared continuum radiation from the dust, the central source, and the cosmic microwave background. The central source represents the dust photosphere separating the inner region where diffusion determines the temperature gradient from the outer region where balance between heating and cooling determines the dust temperature. The input parameters specifying the dust continuum are the dust temperature ($T_{\rm dust}$), the emissivity parameter ($\kappa_{250\mu m}$), the dust frequency dependence (β), and the gas-to-dust mass ratio; while the infrared heating from the central source is defined by the dust photosphere's effective temperature ($T_{\rm star}$) and luminosity.

The spectral energy distribution (SED) and physical structure of G34 was modeled by van der Tak et al. (2013) based on sub-millimeter continuum maps. We adopted their resulting bolometric luminosity and radial profile for the temperature to estimate the infrared continuum radiation from the central source. The dust temperature exponent was adopted from Garay & Rodriguez (1990) and modified together with the source size in order to reproduce $\gtrsim$80% of the observed continuum levels and absorptions in our data, in particular the strong absorption of the 572 GHz transition.

Abundance structure

Variations in the abundance profile of NH_3 in the envelope are governed by gas-grain interactions. At low gas-phase temperatures, molecules are expected to stick to the surfaces of dust grains upon collision, building up mantles dominated by water ice. As temperature increases in the envelope toward the forming star these ices start to evaporate. The binding energy of NH_3 molecules corresponds to complete evaporation at about 30 – 60 K, but since most NH_3 molecules will be trapped in the water ice matrix, only a fraction will be released at these temperatures. At temperatures above 100 K water itself evaporates, baring the grains, and all ammonia can be expected to exist in the gas-phase. In the cold external envelope, where $T < T_{\rm evap,\,NH_3}$, the NH_3 abundance profile is governed by reactions in the gas phase. As a result, the NH_3 abundance is governed by the balance between its formation from N_2H^+, which is mainly destroyed by CO, its freeze-out and its UV photodesorption at the surface of interstellar grains. We have adopted a similar abundance profile for NH_3 in the outer envelope of G34, where $T_{\rm kin} < 100$ K, as modeled by Taquet et al. (in prep.) for low-mass protostars. Due to the different physical conditions between low- and high-mass proto-stars we treat the abundance values in every regime as free parameters. The best-fit abundance profile adopted in our model, as compared to extinction, is shown in Fig. 8.

Table 4: Parameters of the two velocity component ALI model and results.

Parameters held constant		
Distance to source, $d_{\rm source}$	3.3	[kpc]
$V_{\rm LSR}$	58.1	[km s^{-1}]
Envelope size, $R_{\rm max}$	1.8×10^{18}	[cm]
IR-continuum size, $R_{\rm ph}$	7.1×10^{16}	[cm]
Luminosity of source, $L_{\rm bol}$	1.9×10^{5}	[$L_\odot$]
IR-temperature, $T_{\rm star}$	120	[K]
Micro turbulence, $v_{\rm turb}$	1.0	[km s^{-1}]
Gas-to-dust ratio, $M_{\rm gas}/M_{\rm dust}$	100	
Emissivity parameter, $\kappa_{250\mu m}$	10	[cm^2 g^{-1}]
Dust frequency dependence, β	1.7	
Parameters profile[a]		
Temperature, T^b	$15.0\, r^{-0.61}$	[K]
H_2 density, $n(H_2)$		
$r < 0.082$	2.3×10^{6}	[cm^{-3}]
$r > 0.082$	$1.8 \times 10^{4}\, r^{-2.3}$	[cm^{-3}]
Velocity profile, $v_{\rm in}$		
$r < 0.2$	5.1	[km s^{-1}]
$r > 0.2$	2.7	[km s^{-1}]
Results		
$X(NH_3)$		
$r < 0.082$	6.0×10^{-10}	
$r > 0.082$	2.5×10^{-9}	
$N(NH_3)$	3.17×10^{14}	[cm^{-2}]
M(G34)	2 700	[M$_\odot$]
$\dot{M}_{\rm acc}$		
$r = R_{ph}$	4.0×10^{-3}	[M$_\odot$ yr^{-1}]
$r = 0.082 R_{max}$	4.0×10^{-2}	[M$_\odot$ yr^{-1}]
$r = R_{max}$	1.0×10^{-2}	[M$_\odot$ yr^{-1}]

Notes. [a] Normalised radius, $r = R/R_{max}$. [b] T= Kinetic temperature ($T_{\rm K}$) = Dust temperature ($T_{\rm dust}$).

Velocity structure

We use two different velocity fields in our modeling for comparison: *(i)* two clouds, each with a constant velocity (60.8 and 62.8 km s^{-1}) toward the center of the cloud; and, *(ii)* a single gas cloud in free fall similar to the modeling by Wyrowski et al. (2012) and Rolffs et al. (2011) using a free-fall-fraction of $f = 0.3 \pm 0.1$. Here we adjust the mass of the central UC H II in the free-fall velocity M_0 in

$$v = -f \times \sqrt{2GM_{\rm in}/r} \quad (4)$$

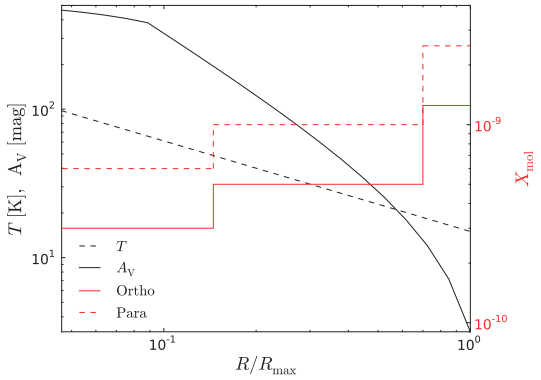

Fig. 8: The resulting ammonia abundance, $X(NH_3)$ and kinetic temperature, T_K profiles obtained in the ALI modeling as a function of the normalized radius of the cloud. The extinction, A_V is measured through the cloud using the corresponding column density of neutral hydrogen atoms, N_H, at different impact distances obtained in the ALI modeling.

where M_{in} is the total (stellar and gas) mass inside radius r. In both scenarios the outflow wing of the 572 GHz line is neglected due to its non-spherical motions. Accordingly, we expect a deeper absorption profile of the model compared with observation.

Density profile

Two sets of radial density profiles are used in the modeling. Both profiles treats the power exponent, p, in $n = n_0\, r^{-p}$ cm^{-3} as a free parameter, where n_0 is the density at R_{max}. The density profile for the first set assumes n to increase continuously all the way towards the center. The second set assumes the density profile to change from exponential to constant at a boundary radius. Both the boundary radius and the constant density are used as free parameters.

5.2. Uncertainties and robustness of the parameters

Even if the reduced chi-square (χ^2) method is only applicable to Gaussian white noise we use χ^2 to get a statistical comparison of the qualities of fits. For each line and model we compute

$$\chi^2_{line} = \frac{1}{n_{ch}} \sum_{i=1}^{n_{ch}} \frac{(o_i - m_i)^2}{\sigma^2} \quad (5)$$

where o_i and m_i are the observed and modeled continuum subtracted intensities, respectively, and n_{ch} the number of channels between 60 and 66 km s^{-1} where the absorption is located. The observational error is dominated by calibration uncertainties (assumed to be 16.4 %, thus representing the band with the highest quadratic combination of noise presented in Sect. 2) rather than by thermal noise which is <10 %. Therefore σ represents the calibration uncertainty multiplied with the maximum intensity in the spectra (with continuum). This method is adopted from Rolffs et al. (2011). If $\chi^2 \sim 1$ the model matches the observations very well, if less than unity the noise is overestimated, and, if larger than unity the fit do not capture the features of the observed line profile or the noise has been under estimated. The high χ^2 values in our best fit is most likely due to our low noise levels and high continuum rather than a poor fit.

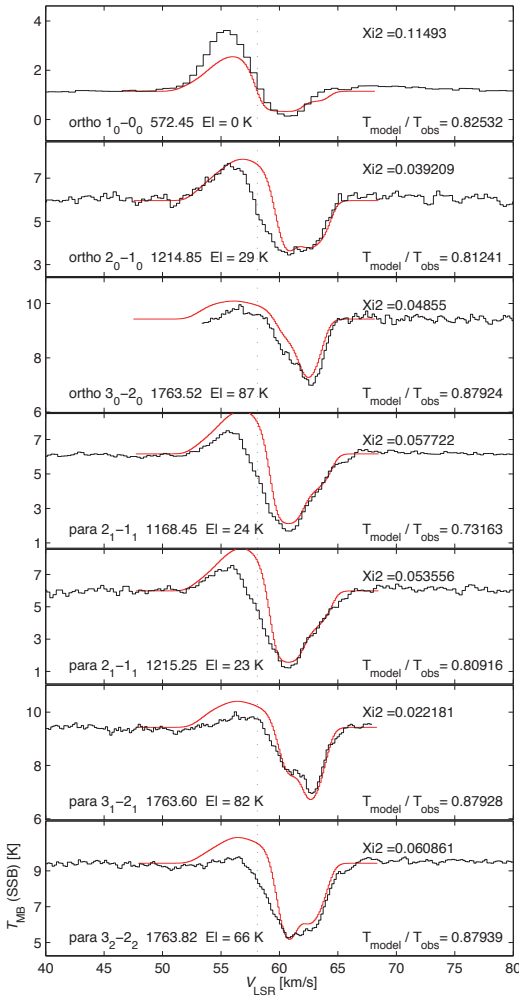

Fig. 9: Observed *Herschel*-HIFI spectra in black compared to the resulting model line profiles in red. We have shifted the modeled continuum to the observed value to allow comparisons. The ratio of the modeled and observed continuum at the frequency of each line is given in respective legend.

6. Discussion

The large inward velocities at the large radii traced by the ammonia absorptions suggests that G34 is far from a typical star-forming region. Consequently our attempts to model the absorption line profiles with a single velocity field failed. When employing a free-fall velocity field we found that the absorption at the higher velocities in all observed absorption line profiles are strongly underestimated when implementing the free-fall-fraction values of 0.2 and 0.3 used by Wyrowski et al. (2012)

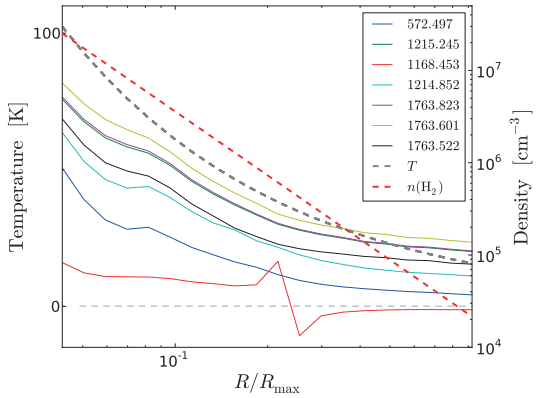

Fig. 10: The modeled excitation temperatures as a function of the normalized radius. We use the same color code as in Fig. 2. (A negative T_{ex} corresponds to a maser transition.)

and Rolffs et al. (2011) (example shown in Fig. A.1). In order to produce an acceptable fit (shown in Fig. A.2), an unrealistically high mass of the order of ∼2000 $M_\odot$ of the ultra compact H II region was required, in contrast to the observational mass estimates of 76 – 360 $M_\odot$ (Liu et al. 2013; Watt & Mundy 1999; Garay et al. 1986).

Our modeling do, however, confirm the scenario where *two* gas clouds are moving inwards toward the central region of G34 each with a constant velocity. The best fit model suggests velocities of ∼ 2.7 and ∼ 5.1 km s^{-1} higher than the source systemic velocity, a slightly higher velocity than predicted for the second cloud component.

The line profiles could not be modeled with a constant or radially continuous profile of the molecular hydrogen density (example shown in Fig. A.3). We were instead able to improve the fit to both the emission and absorption profiles with a step-wise model of the molecular hydrogen density: a constant and slightly lower density distribution deep inside the molecular cloud, and exponentially decreasing outwards.

Our best-fit model is shown in Fig. 9 with comparison observational data, and the parameters used are listed in Table 4. We also plot the modeled T_{ex}, T_K and $n(H_2)$ as a function of normalised radius in Fig. 10.

Six of the absorption line profiles are very well reproduced at velocities ∼61 – 65 km s^{-1}. The emission components in five lines are, however, somewhat overestimated. One of the major problems in the modeling was the fundamental ortho 572 GHz line which we were not able to accurately model simultaneously as the higher excited transitions. In the best fit model to all lines, we found both too little emission and too little absorption in this line. We speculate that this is due to our assumed simplifications of the source structure since the source is known to have a very different shape than our assumed spherical geometry on the large scales where most likely bulk of the emission and absorption of the 572 GHz line is produced.

Our best model suggests an ammonia abundance of 6.0×10^{-10} and 2.5×10^{-9} in the inner and outer regions, respectively. The ortho-to-para ratio of ammonia is 0.5 throughout the whole cloud which is similar to the values found in the sight-lines toward W31C and W49N (Persson et al. 2012). The low ammonia abundance in the inner region is interpreted to be caused by the enhanced extinction in the cold region (T_K < 100 K). In the outer region, the abundance may be enriched from ice sublimation by UV photodesorption. Comparing with the chemical models presented in Persson et al. (2014) the low derived abundances suggests that the molecular gas is not yet in steady state with an age of approximately 10^5 years also recently derived by Coutens et al. (2014).

6.1. Mass accretion rate

The total mass within our modeled radius is M_{G34} = 2700 $M_\odot$, ∼50% higher than the 1800 $M_\odot$ found by van der Tak et al. (2013) modeling low-excitation water lines. The mass in each shell of our model is like gas clumps moving inwards at a constant velocity which depends on the location in the molecular cloud. These gas clumps can become accreted by the cluster of stars forming in G34 if the accretion rate is higher than the outwards directed radiation pressure from the luminous proto-stars. If this is the case, this star forming scenario would agree with the Bonnell et al. (1997, 2001) competitive accretion model. This model refers to the fact that the distances between the proto-stars in a massive cluster is typically less than the size of the accreting envelope such that they must "compete" for the reservoir of material.

The mass accretion rate is estimated by first making a rough estimate if the gas is undergoing spherically symmetric free-fall collapse at any radius. Then the mass accretion rate $\dot{M}_{acc}$ is estimated from the infall velocity, v_{infall}, by applying the method described by Beltrán et al. (2006). At any radius R, the mass accretion rate is given by

$$\dot{M}_{acc} = 4\pi R^2 m_{H_2} n_{H_2} v_{infall} \; [M_\odot \, km \, s^{-1}], \quad (6)$$

where m_{H_2} is the mass of the H_2 molecule, n_{H_2} is the gas volume density of molecular hydrogen, and v_{infall} is the infall velocity as a function of the radius R as described in Table. 4. When the velocity increases to 5.1 km s^{-1} radially inwards, the mass accretion rate is not constant with radius and reaches its maximum at the radius of $0.082R_{max}$ just before the profile of n_{H_2} decreases down to 2.3×10^6 [cm^{-3}]. In the innermost modeled shell (R_{ph}, the surface of the IR-continuum object) where the infall velocity is unchanged at 5.1 km s^{-1} but the density significantly lower, leads to a lower mass accretion rate according to Eq. 6.

Using Eq. 6, the inferred mass accretion rate at R_{ph} becomes 4.0×10^{-3} $M_\odot yr^{-1}$. At $0.082R_{max}$, where the number density and velocity is the highest, the mass accretion rate becomes 4.0×10^{-2} $M_\odot yr^{-1}$. In the outer envelope, at R_{max}, the infall velocity is 2.7 km s^{-1} and the corresponding mass accretion rate is then 1×10^{-2} $M_\odot yr^{-1}$, supporting the estimates by Wyrowski et al. (2012) and Liu et al. (2013) in the outer envelope.

These mass accretion rates are high enough (> 10^{-3} $M_\odot yr^{-1}$) to quench any H II region (Walmsley 1995; Wolfire & Cassinelli 1987) and to overcome the radiation pressure from the forming (proto) cluster. The accretion in the inner envelope appears to be halted, which is mainly due to the slightly lower density distribution in the inner most region of the molecular cloud, see Table. 4. This suggests that the gas clumps from the outer envelope first accretes onto this inner region, are halted, and then continues its inward motion to the central objects. Despite this drop of accretion, such high infall velocities and mass infall rates are expected for more evolved massive star forming regions compared with the stages prior to the hot core phase (Liu et al. 2013).

These results demonstrates that rotational ammonia transitions seen in absorption toward a strong far-infrared continuum

source can successfully be used to probe infall velocities, physical and chemical properties in a variety of evolutionary stages of massive star forming clumps.

Acknowledgements. The Herschel spacecraft was designed, built, tested, and launched under a contract to ESA managed by the Herschel/Planck Project team by an industrial consortium under the overall responsibility of the prime contractor Thales Alenia Space (Cannes), and including Astrium (Friedrichshafen) responsible for the payload module and for system testing at spacecraft level, Thales Alenia Space (Turin) responsible for the service module, and Astrium (Toulouse) responsible for the telescope, with in excess of a hundred subcontractors. HIFI has been designed and built by a consortium of institutes and university departments from across Europe, Canada and the United States under the leadership of SRON Netherlands Institute for Space Research, Groningen, The Netherlands and with major contributions from Germany, France and the US. Consortium members are: Canada: CSA, U.Waterloo; France: CESR, LAB, LERMA, IRAM; Germany: KOSMA, MPIfR, MPS; Ireland, NUI Maynooth; Italy: ASI, IFSI-INAF, Osservatorio Astrofisico di Arcetri-INAF; Netherlands: SRON, TUD; Poland: CAMK, CBK; Spain: Observatorio Astronmico Nacional (IGN), Centro de Astrobiologa (CSIC-INTA). Sweden: Chalmers University of Technology - MC2, RSS & GARD; Onsala Space Observatory; Swedish National Space Board, Stockholm University -Stockholm Observatory; Switzerland: ETH Zurich, FHNW; USA: Caltech, JPL, NHSC. MH, CMP, JHB and ESW acknowledge generous support from the Swedish National Space Board.

References

Beltrán, M. T., Cesaroni, R., Codella, C., et al. 2006, Nature, 443, 427
Bergin, E. A. & Langer, W. D. 1997, ApJ, 486, 316
Beuther, H. 2007, ArXiv e-prints
Beuther, H., Schilke, P., Menten, K. M., et al. 2002, ApJ, 566, 945
Biver, N., Crovisier, J., Bockelée-Morvan, D., et al. 2012, A&A, 539, A68
Bjerkeli, P., Liseau, R., Nisini, B., et al. 2011, A&A, 533, A80
Bonnell, I. A., Bate, M. R., Clarke, C. J., & Pringle, J. E. 1997, MNRAS, 285, 201
Bonnell, I. A., Bate, M. R., Clarke, C. J., & Pringle, J. E. 2001, MNRAS, 323, 785
Cazzoli, G., Dore, L., & Puzzarini, C. 2009, A&A, 507, 1707
Cesaroni, R., Galli, D., Lodato, G., Walmsley, C. M., & Zhang, Q. 2007, Protostars and Planets V, 197
Cesaroni, R., Walmsley, C. M., & Churchwell, E. 1992, A&A, 256, 618
Cheung, A. C., Rank, D. M., Townes, C. H., Thornton, D. D., & Welch, W. J. 1968, Physical Review Letters, 21, 1701
Coutens, A., Vastel, C., Hincelin, U., et al. 2014, MNRAS, submitted
Danby, G., Flower, D. R., Valiron, P., Schilke, P., & Walmsley, C. M. 1988, MNRAS, 235, 229
de Graauw, T., Helmich, F. P., Phillips, T. G., et al. 2010, A&A, 518, L6
Faure, A., Hily-Blant, P., Le Gal, R., Rist, C., & Pineau des Forêts, G. 2013, ApJ, 770, L2
Flagey, N., Goldsmith, P. F., Lis, D. C., et al. 2013, ApJ, 762, 11
Garay, G. & Rodriguez, L. F. 1990, ApJ, 362, 191
Garay, G., Rodriguez, L. F., & van Gorkom, J. H. 1986, ApJ, 309, 553
Hatchell, J., Thompson, M. A., Millar, T. J., & MacDonald, G. H. 1998, A&AS, 133, 29
Hily-Blant, P., Maret, S., Bacmann, A., et al. 2010, A&A, 521, L52
Hjalmarson, Å., Bergman, P., Biver, N., et al. 2005, Advances in Space Research, 36, 1031
Ho, P. T. P. & Townes, C. H. 1983, ARA&A, 21, 239
Hoare, M. G. 2005, Ap&SS, 295, 203
Keene, J., Blake, G. A., & Phillips, T. G. 1983, ApJ, 271, L27
Larsson, B., Liseau, R., Bergman, P., et al. 2003, A&A, 402, L69
Liu, T., Wu, Y., & Zhang, H. 2013, ApJ, 776, 29
Maercker, M., Schöier, F. L., Olofsson, H., Bergman, P., & Ramstedt, S. 2008, A&A, 479, 779
Maret, S., Faure, A., Scifoni, E., & Wiesenfeld, L. 2009, MNRAS, 399, 425
Moscadelli, L., Cesaroni, R., Sánchez-Monge, Á., et al. 2013, A&A, 558, A145
Nordh, H. L., von Schéele, F., Frisk, U., et al. 2003, A&A, 402, L21
Olmi, L. & Cesaroni, R. 1999, A&A, 352, 266
Ott, S. 2010, in Astronomical Society of the Pacific Conference Series, Vol. 434, Astronomical Data Analysis Software and Systems XIX, ed. Y. Mizumoto, K.-I. Morita, & M. Ohishi, 139
Pauls, T. & Wilson, T. L. 1980, A&A, 91, L11
Persson, C. M., De Luca, M., Mookerjea, B., et al. 2012, A&A, 543, A145
Persson, C. M., Hajigholi, M., Hassel, G. E., et al. 2014, A&A, submitted
Persson, C. M., Olberg, M., . Hjalmarson, Å., et al. 2009, A&A, 494, 637
Pickett, H. M., Poynter, R. L., Cohen, E. A., et al. 1998, J. Quant. Spec. Radiat. Transf., 60, 883
Pilbratt, G. L., Riedinger, J. R., Passvogel, T., et al. 2010, A&A, 518, L1
Rist, C., Alexander, M. H., & Valiron, P. 1993, J. Chem. Phys., 98, 4662
Roelfsema, P. R., Helmich, F. P., Teyssier, D., et al. 2012, A&A, 537, A17
Rolffs, R., Schilke, P., Wyrowski, F., et al. 2011, A&A, 527, A68
Rybicki, G. B. & Hummer, D. G. 1991, A&A, 245, 171
Rybicki, G. B. & Hummer, D. G. 1992, A&A, 262, 209
Shepherd, D. S., Claussen, M. J., & Kurtz, S. E. 2001, Science, 292, 1513
Sollins, P. K., Zhang, Q., Keto, E., & Ho, P. T. P. 2005, ApJ, 624, L49
van der Tak, F. F. S., Chavarría, L., Herpin, F., et al. 2013, A&A, 554, A83
Walmsley, M. 1995, in Revista Mexicana de Astronomia y Astrofisica, vol. 27, Vol. 1, Revista Mexicana de Astronomia y Astrofisica Conference Series, ed. S. Lizano & J. M. Torrelles, 137
Walsh, A. J., Burton, M. G., Hyland, A. R., & Robinson, G. 1998, MNRAS, 301, 640
Watt, S. & Mundy, L. G. 1999, ApJS, 125, 143
Wirström, E. S., Bergman, P., Black, J. H., et al. 2010, A&A, 522, A19
Wolfire, M. G. & Cassinelli, J. P. 1987, ApJ, 319, 850
Wyrowski, F., Güsten, R., Menten, K. M., Wiesemeyer, H., & Klein, B. 2012, A&A, 542, L15
Yorke, H. W. & Sonnhalter, C. 2002, ApJ, 569, 846
Zhang, Q. & Ho, P. T. P. 1997, ApJ, 488, 241
Zhang, Q., Hunter, T. R., & Sridharan, T. K. 1998, ApJ, 505, L151
Zinnecker, H. & Yorke, H. W. 2007, ARA&A, 45, 481

Appendix A: ObsID of Herschel observations

Table A.1: G34.26+0.15: *Herschel*-HIFI OBSID's of the observed transitions analysed in this paper.

Specie	Frequency (GHz)	Band[a]	LO-setting[b]	Date	OBSID
o-NH_3	572.498	1b (USB)	A	2011-04-22	1342219281
			B		1342219282
			C		1342219283
	1214.852	5a (USB)	A	2011-03-13	1342215886
			B		1342215884
			C		1342215885
	1763.524	7a (USB)	A	2012-04-20	1342244604
			B		1342244605
			C		1342244606
p-NH_3	1215.245	5a (USB)	A	2011-04-22	1342215886
			B		1342215884
			C		1342215885
	1168.454	5a (LSB)	A	2012-04-18	1342244518
			B		1342244517
			C		1342244519
	1763.824	7a (USB)	A	2011-04-20	1342244604
			B		1342244605
			C		1342244606
	1763.602	7a (USB)	A	2011-04-20	1342244604
			B		1342244605
			C		1342244606

Notes. [(a)] HIFI consists of 7 different mixer bands and two double sideband spectrometers (USB is the upper sideband, and LSB is the lower sideband). [(b)] Three different frequency settings of the LO were performed, with approximately 15 km s^{-1} between each setting in order to determine the sideband origin of the signals.

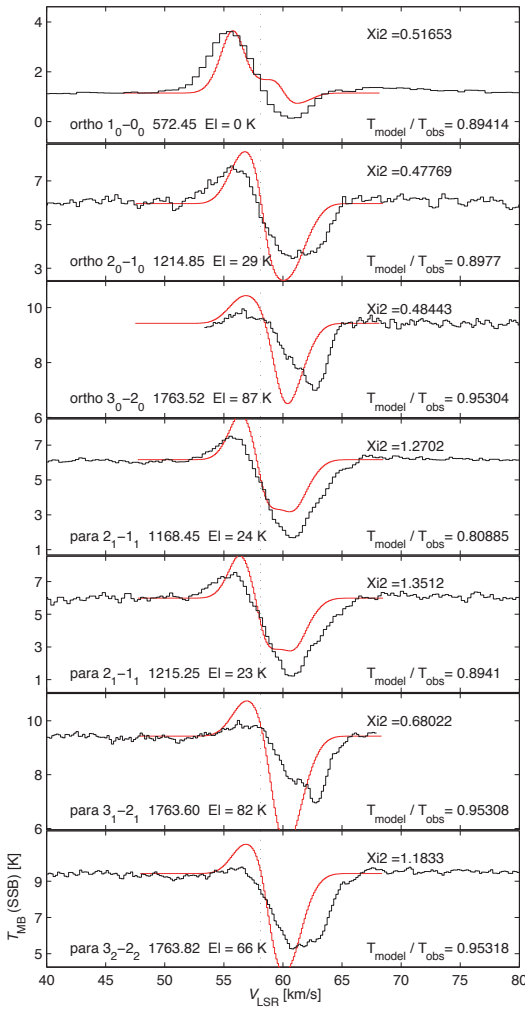

Fig. A.1: ALI: *Free-fall* using a free fall fraction of 0.3 and M_0 = 350 $M_\odot$. Notation as in Fig. 9.

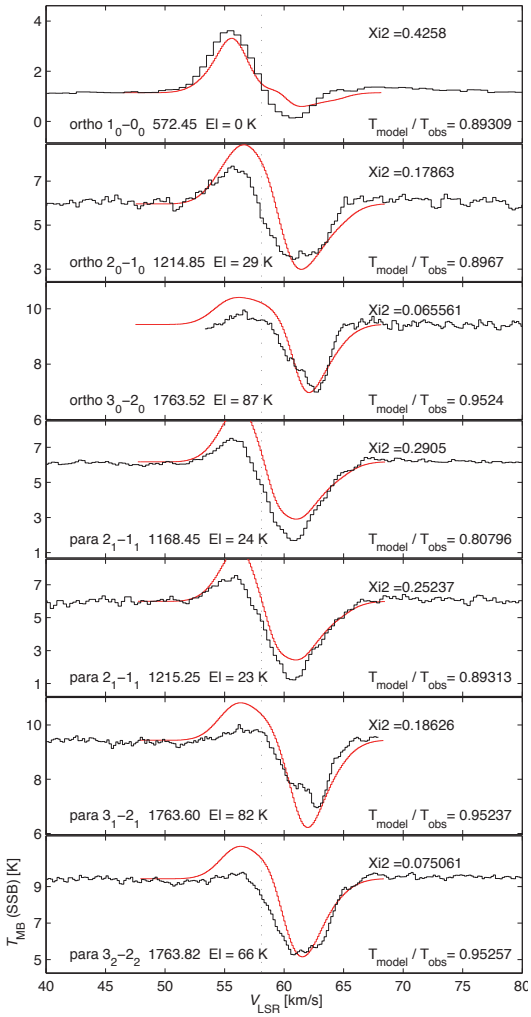

Fig. A.2: ALI: *Free-fall* using a free fall fraction of 0.7 and M_0 = 1 000 $M_\odot$. Notation as in Fig. 9.

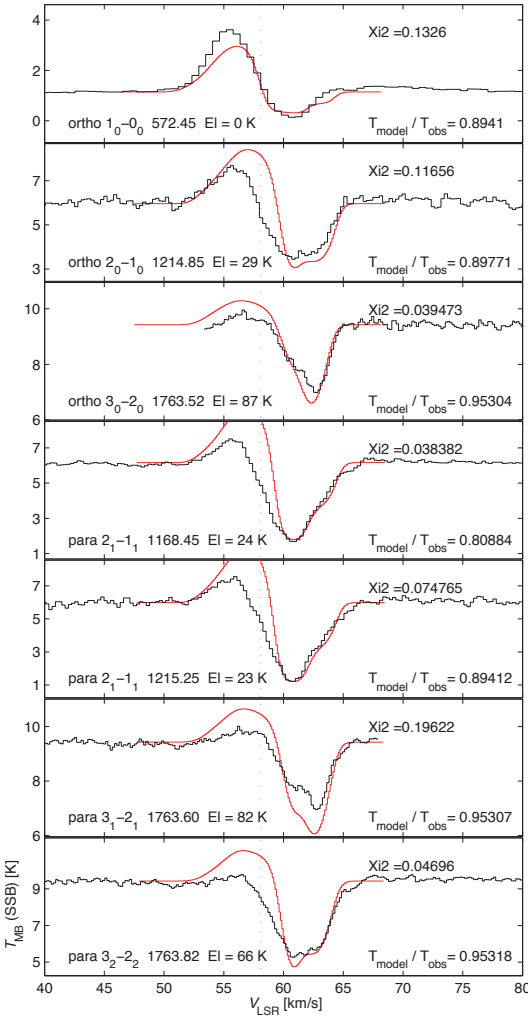

Fig. A.3: ALI: one radial continuous density profile. Notation as in Fig. 9.